



Acoustic backscattering at a tidal intrusion front

Christopher Bassett^{a,*}, Andone C. Lavery^b, David Ralston^b, W. Rockwell Geyer^b,
Joseph T. Jurisa^c, Jim Thomson^a, David A. Honegger^d, Alexandra Simpson^{d,e},
Malcom E. Scully^b, Merrick C. Haller^d

^a Applied Physics Laboratory, University of Washington, 1013 NE 40th St, Seattle, 98105, Seattle, USA

^b Woods Hole Oceanographic Institution, Woods Hole, 02543, MA, USA

^c Horn Point Laboratory, University of Maryland, Cambridge, 21613, MD, USA

^d Oregon State University, Corvallis, 97331, OR, USA

^e Scripps Institution of Oceanography, University of California–San Diego, San Diego, CA 92093-0206, USA

ARTICLE INFO

Keywords:

Acoustic backscattering
Broadband echosounders
Estuary
Front
Bubbles
Microstructure
Stratification
Sediment
James river
Virginia
USA

ABSTRACT

Strong spatial gradients and rapidly evolving, three-dimensional structure make estuarine fronts difficult to sample. Echosounders can be used near fronts to provide nearly synoptic images of water column processes and, with sufficient bandwidth, can provide quantitative information about dynamical variables derived from forward and inverse methods using acoustic backscattering measurements. This manuscript discusses measurements using broadband (50–420 kHz) echosounders from the James River (Virginia, USA) tidal intrusion front. The dominant backscattering mechanisms observed at the site include bubbles, turbulent microstructure, interfaces associated with stratification, suspended sediment, and biota. Existing analytical models are used to interpret contributions from these sources with acoustic inversions providing quantitative information about the physical structure and processes that compare favorably with conventional, in situ measurements. Supporting data sets for this analysis include measurements of temperature, salinity, velocity, and turbidity; X-band radar images of sea surface roughness; aerial optical imagery; Lagrangian measurements of waves, turbulence, and velocity structure; and Regional Ocean Modeling System circulation model simulations. A notable advantage of acoustic remote sensing is the ability to resolve processes at considerably higher spatial resolution (< 1 m horizontal; < 5 cm vertical) than other in situ sampling approaches.

1. Introduction

A common feature where rivers discharge into coastal oceans is the presence of sharp fronts that represent intensified gradients in density and velocity that are usually strongly time- and space-dependent (Wright and Coleman, 1971; Yankovsky and Chapman, 1997). A tidal river plume is the expanding volume of buoyant water that spreads offshore along the surface of the ocean during ebb tides. In contrast, during flood tides when the inflow of dense waters is strong enough to arrest the outflow of buoyant estuarine waters, a tidal intrusion front is formed as the denser water is subducted under the plume (Simpson and Nunes, 1981; Largier, 1992). Strong convergence zones are observed in both ebb plumes and tidal intrusion fronts, and the frontal boundaries often have readily observed surface expressions. Horizontal gradients in water properties across fronts are dependent on factors including, but not limited to, tidal forcing, river discharge, coastal currents, wind, ambient stratification, channel geometry, and bathymetry (Horner-Devine et al., 2015).

The conditions that emerge in relatively energetic, estuarine environments provide a unique opportunity for leveraging high-frequency acoustic backscattering (ABS) techniques in support of traditional physical sampling approaches. Specifically, while physical sampling techniques undersample many processes, the high spatial and temporal resolution of ABS measurements can be used for synoptic imaging purposes and, to a lesser degree, to quantify and discriminate between processes of interest. When coupled with the optimal sampling frequencies, these benefits are derived from frequency-dependent scattering associated with processes of interest.

For decades, ABS techniques have been used to image physical processes and structures in open ocean and estuarine environments (Yakuwa and Ohtani, 1969; Hauray et al., 1979). While focused on a broad range of applications, these studies generally fall into two main categories. First, the relatively high sampling resolution in both the vertical and horizontal are used to provide qualitative support for the broader scientific objective of the study. In these cases, the primary

* Corresponding author.

E-mail address: cbassett@uw.edu (C. Bassett).

<https://doi.org/10.1016/j.pocean.2023.103167>

Received 14 February 2023; Received in revised form 28 September 2023; Accepted 4 November 2023

Available online 8 November 2023

0079-6611/© 2023 The Author(s). Published by Elsevier Ltd. This is an open access article under the CC BY license (<http://creativecommons.org/licenses/by/4.0/>).

benefit is the ability to rapidly generate images (echograms) from scattering in the water column. The second major category of ABS studies is associated with the quantification of processes and variables of interest. This may include simply using images to better quantify scales of interest. Other studies apply physical measurements in forward and inverse methods using scattering models to derive information from the intensity and frequency dependence of ABS. In general, forward models are used to predict backscattering based on a set of measured or assumed properties of scatterers. Inverse methods, on the other hand, are used to estimate properties or quantities of a scatterer based on the measured intensity and frequency dependence.

In addition to their wide use in fisheries and ecological studies, other topics studied with the support of ABS measurements include bubbles (Medwin, 1977b; Thorpe et al., 1994; Dahl and Jessup, 1995; Vagle and Farmer, 1992; Baschek et al., 2006), hydraulic transitions (Farmer and Dungan Smith, 1980; Cummins et al., 2006), suspended sediment (Young et al., 1982; Hay, 1983; Hanes et al., 1988; Thorne et al., 1991, 2014; Thorne and Hurther, 2014), internal waves (Hauray et al., 1979; Farmer and Armi, 1999; Orr et al., 2000; Moum et al., 2003), and microstructure (Hauray et al., 1979; Thorpe and Brubaker, 1983; Seim et al., 1995; Seim, 1999; Ross and Lueck, 2003; Warren et al., 2003; Lavery et al., 2010a,b, 2013; Ross and Lavery, 2011; Duda et al., 2016). Many of these references, and others therein, provide a basis for using multi-channel ABS measurements for scattering source attribution and quantification using the frequency responses of different scattering mechanisms.

In estuarine environments ABS from acoustic Doppler current profilers (ADCPs) (Jay et al., 2009; Pan and Jay, 2009a,b; Horner-Devine and Chickadel, 2017) and echosounders (Farmer and Dungan Smith, 1980; Baschek et al., 2006; Kilcher and Moum, 2010; Geyer et al., 2010; Holleman et al., 2016) has been used to image river plumes and internal structure. However, the use of forward and inverse models to make quantitative inferences using these data has been more limited. Exceptions include the measurements of Trump and Marmorino (2003), Kilcher and Moum (2010), and Mazzini and Chant (2016), in which the backscatter from each of the four ADCP beams was used to investigate the along-front variability in ABS. Further adoption of acoustic backscattering measurements holds significant potential to increase the amount of information that can be obtained when sampling the rapidly evolving water column in many estuarine environments.

This study uses high-frequency ($f > 10$ kHz) acoustic backscattering (ABS) at a tidal intrusion front to study the intensity and distribution of backscattering sources that are common in estuaries. These include bubbles, biota, suspended sediment, turbulent microstructure, and interfaces associated with sharp gradients in the acoustic properties of the water column. By combining echosounder measurements, scattering models, and physical oceanographic data, we demonstrate the quantitative and qualitative potential of ABS measurements in studies of estuarine systems. Motivating this work is the hypothesis that advances in off-the-shelf echosounder systems and analytical models make ABS techniques an essential tool for estuarine scientists. These techniques, however, cannot replace physical sampling which is required to both constrain acoustic models and determine where processes of interest may overlap and result in mixed-frequency responses.

The James River (Virginia, USA) tidal intrusion front is the focus of this work. In this study, echosounders are deployed from a small research vessel. These shipboard measurements provide a platform with coincident conductivity, temperature, and depth (CTD), velocity, and ABS measurements. Supporting measurements include Lagrangian surface drifters, an X-band radar, a drone equipped with optical cameras, a moored acoustic Doppler current profiler and CTD, and sediment cores. Collectively, these instruments provide a comprehensive view of processes observed in the estuary.

The paper begins with an overview of the methods used for collecting the acoustic and supporting measurements. Next, we provide an overview of the dominant scattering mechanisms, relevant analytical

and empirical models, and constraints on model parameters derived from in situ measurements. This section also includes a summary of acoustic data processing techniques. Next, the results are presented with context provided by the in situ and remote sensing instrumentation. The paper concludes with a summary of findings from the James River and a discussion of the capabilities and limitations of echosounders, with considerations for their broader applicability to studies in other estuarine environments.

The main focus of the paper is backscattering from physical oceanographic sources. Methods and results related to biological scatterers are included as supplemental material. While generally important, biological sources did not dominate the measured backscattering in this study. In addition, the methodology used to quantify biological backscattering from lakes to open ocean environments is well-established (Simmonds and MacLennan, 2005). With the inclusion of biological backscattering, this paper presents a comprehensive overview of water column ABS observed in the vicinity of the James River tidal intrusion front.

2. Methods

2.1. Site description and experiment

The James River, Virginia (USA) is a tributary that discharges into the southern end of Chesapeake Bay. Throughout the tidal cycle, the lower James River waters remain brackish tens of kilometers upriver from the mouth (Pritchard, 1952). Depths in the main channel within the study area are 15 to 20 m with surrounding shoals less than 10 m deep (Fig. 1). Within the study area, the Monitor–Merrimac Memorial Bridge–Tunnel extends north to south across the river. Directly above the tunnel is a bathymetric depression that provides a source of bathymetric forcing.

Intensive sampling of flood tides near the mouth of the James River was performed from 20–25 April 2019 with a focus on the tidal intrusion front. This front is the surface expression associated with the salt wedge formed as the denser waters of Chesapeake Bay propagate upriver. The instruments used in this analysis included a research vessel with numerous sensor packages, a mooring, Lagrangian drifters, and air-side sensors, which are described in detail in the following sections. Sampling on 21, 22, and 25 April was performed along the thalweg and 23–24 April sampling was dedicated to cross-channel measurements (Fig. 1). All data related to vessel transects were mapped onto an along- and cross-channel coordinate system with the origin over the tunnel.

2.2. In situ instrumentation

In situ sampling included a mooring, ship-based downward-looking echosounders and an ADCP, a towed array, a free-falling profiler, and instrumented Lagrangian drifters.

2.2.1. Mooring

An instrumented tripod was deployed on the seabed at $36^{\circ} 57.274'N$, $76^{\circ} 24.712'W$ (Fig. 1). The mooring had an upward-looking Nortek Signature500 ADCP and an RBRconcerto CTD logger equipped with a Seapoint Turbidity Meter to measure optical backscatter (OBS). The ADCP was deployed 0.92 m above the seabed and sampled at 8 Hz in 0.5 m bins. Data were processed to produce 10-s and 1-min average profiles of the horizontal and vertical water velocities. CTD and OBS data were logged at 0.2 Hz approximately 0.5 m above the seabed.

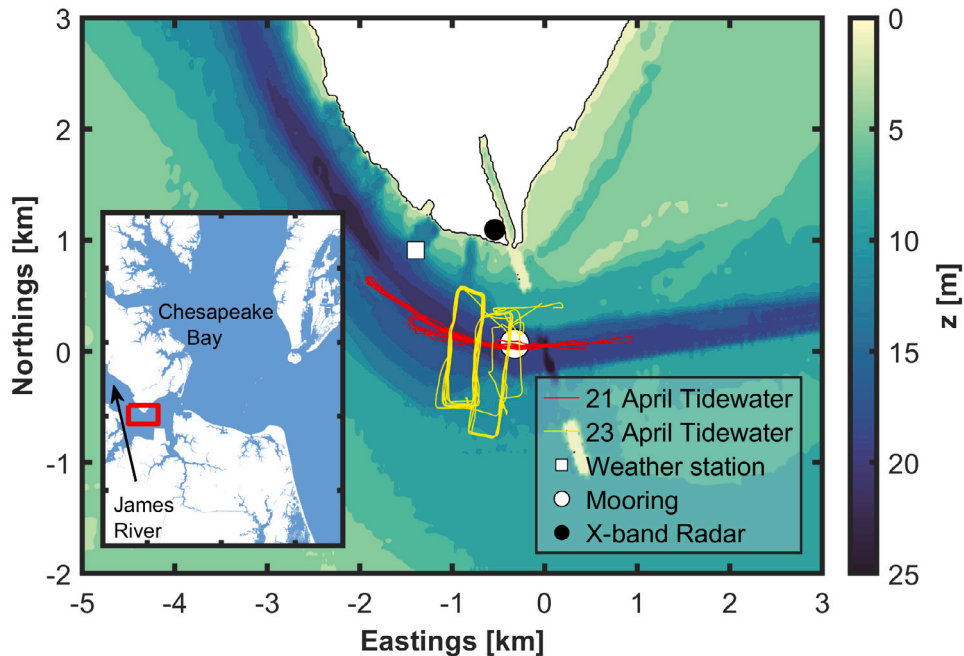


Fig. 1. The James river study site. The colored lines show vessel transects during along- and cross-channel sampling on 21 and 23 April 2019. Dots show the locations of fixed instrumentation packages and the National Buoy Data Center Dominion Terminal weather station. (Inset) The site's location within the Chesapeake Bay region.

2.2.2. Lagrangian drifters

Four Lagrangian drifters, referred to as SWIFTs (Thomson et al., 2019), with downward-looking Nortek Signature1000 ADCPs, conductivity and temperature sensors, air-side optical cameras, and meteorological sensors were deployed throughout the experiment. The SWIFTs were deployed in the Chesapeake Bay waters and drifted with the flooding currents until recovered and redeployed. All of the sensors onboard the SWIFTs record raw data at 5 Hz in bursts lasting 512 s, followed by 208 s for onboard processing and Iridium telemetry. Statistical products for each 512-second burst, in addition to shorter averaging periods of 60 s and 10 s, include turbulence dissipation rate profiles, velocity profiles, surface wave parameters and spectra, surface wind speed and direction, mean water temperatures and salinities, and time-lapse videos.

The downward-looking Nortek Signature1000 profiles from the SWIFTs utilize two modes. In the first, four slant beams are used in a broadband Doppler mode to produce profiles of the currents with 0.5 m bins from 0.35 to 19.85 m. The profiles are corrected for the drift and motion of the platform using an onboard Global Positioning System (GPS) receiver and Inertial Motion Unit (IMU), such that the final products are east-north-up components of the currents in a fixed geographic reference frame. In the second mode, the fifth vertical beam is used in a pulse-coherent Doppler mode for high-resolution (HR) profiles with 0.04 m bins from 0.12 to 2.64 m. These are processed in the drifting reference frame using a structure function to determine turbulent dissipation rates (Thomson, 2012).

2.2.3. Vessel-based instrumentation

Ship-based measurements were obtained using *R/V Tidewater*, a 13 m vessel operated by the Virginia Institute of Marine Science. Four Simrad broadband transducers (ES70-7CD, ES120-7CD, ES200-7CD, and ES333-7CD) and a 1200 kHz RDI Workhorse ADCP were pole-mounted and deployed starboard, midship approximately 0.5 m below the surface. The transducers were driven by two Simrad WBT Tube transceivers with 1 ms pulse durations and bandwidths of 50–90 kHz, 95–155 kHz, 160–260 kHz, 280–420 kHz, respectively. Transmit power settings were 500 W, 240 W, 150 W, and 50 W, respectively. Pulse repetition rates were between 5 Hz and 10 Hz throughout the experiment.

All channels were operated synchronously in “high-resolution” mode, meaning that the typical second-stage decimation (Demer et al., 2017) was not applied and raw data were stored at 250 kHz.

An array of seven RBR CTDs spaced at 2 m intervals and sampling at 1 Hz was deployed from the vessel's starboard quarter using the A-frame and a winch for control. The array was deployed in-line with an instrumented tow body that “flew” near the seabed. This line was raised and lowered as necessary to avoid grounding. Another RBR CTD with an OBS sensor (16 Hz sampling rate) was mounted to a frame with a custom logger operating a Rockland Scientific Microsquid microstructure sensor (temperature and conductivity; 512 Hz sampling rate). This free-falling system was operated continuously using a manually controlled winch on the aft deck of the vessel to measure profiles throughout the water column every one to two minutes. Profiler data was processed for temperature and salinity profiles, the buoyancy frequency, dissipation rate of turbulent kinetic energy (ϵ), and dissipation rate of turbulent salinity variance (χ_S) following established methods (Nash and Moum, 2002; Holleman et al., 2016) assuming a mixing efficiency of 0.2.

2.3. Remote sensing observations

Microwave backscatter intensity observations were acquired with an imaging X-band marine radar ($36^\circ 57.798'N$, $76^\circ 24.882'W$) mounted atop a telescoping tower 35 m above sea level. The radar was equipped with a 3-m long horizontally polarized antenna that completed a 360° sweep of the area in 1.36 s (44 RPM). Transmit pulses, which were 80 ns in duration with a pulse repetition frequency of 2000 Hz, were first oversampled in range with 3 m spacing from the inherent radar resolution of ~ 12 m. Sets of four sequential pulses were averaged to reduce noise and then interpolated to a polar grid (3 m by 0.5°). Finally, a pointwise moving time average of 64 rotations (80 s) was applied to remove surface wave signals and enhance the longer time scale frontal imaging. Front position was marked by enhanced uncalibrated return intensity in the resulting time exposure image owing to a persistently rough sea surface and frequent small-scale wave breaking events. Similar observations and associated methodology from a study in the

Columbia River (USA) are reported in [Honegger et al. \(2017\)](#) and the full system description is given in [Haller et al. \(2019\)](#).

A Yuneec H520-G hexacopter equipped with a Yuneec E90 optical camera was used for collecting optical RGB imagery during the experiment. The small Unpiloted Aircraft System (sUAS) was flown from a pier on the north shore of the river channel, near the X-Band radar tower, with a flight radius up to 1 km. Imagery of the front was collected over four days throughout the flood tide. Video was collected at 60 frames per second with bookend snapshots utilized for their exchangeable image file data of sUAS location. The extrinsic camera parameters can be used for rectification of footage collected at nadir but the recorded camera angle did not have enough certainty to rectify non-nadir imagery. This study utilizes oblique imagery collection by the sUAS for high-resolution, qualitative information of frontal characteristics.

2.4. ROMS model

Numerical simulations were conducted using the Regional Ocean Modeling Systems (ROMS) ([Haidvogel et al., 2008](#)) and a high-resolution grid (17 m by 17 m horizontal resolution) of Newport News Point including the Monitor–Merrimac Memorial Bridge–Tunnel complex. This high-resolution model was forced along the open boundaries using the output from a larger-scale (50 m by 50 m horizontal resolution) model of the James River estuary, which was nested within a model of the entire Chesapeake Bay (360 m by 360 m horizontal resolution). The large-scale model of Chesapeake Bay has nearly identical forcing to the model used in [Scully \(2016\)](#), but employs a new grid with increased horizontal resolution to better facilitate nesting. The high-resolution grid of Newport News Point employed 30 terrain following sigma coordinates and achieved turbulence closure using the k-omega model with the stability functions of [Kantha and Clayson \(1994\)](#). The background diffusivity for both momentum and scalars was set to $1 \cdot 10^{-6}$ m²/s and no horizontal diffusion was prescribed. Local wind forcing for the simulations was obtained from the direct observations collected at the National Buoy Data Center Dominion Terminal (DOMV2) station ([Fig. 1](#)).

3. Dominant scattering mechanisms and acoustic data processing

Five common sources of backscatter emerged from the acoustic analysis of the James River tidal intrusion front and the surrounding waters. The identified sources were (i) bubbles subducted by downwelling currents at the convergence of the Chesapeake Bay and James River waters, (ii) turbulent microstructure associated with shear instabilities, (iii) interfaces, (iv) suspended sediment, and (v) fish. Contributions of these ABS sources varied spatially relative to the front location and temporally both within the tidal cycle and with spring/neap variability in tidal amplitude. The following sections present analytical models for these sources of backscattering and the steps applied to use them in forward and inverse models. For reference, [Fig. 2](#) provides examples of volume backscattering measurements from three of the common sources of acoustic backscattering in the vicinity of the tidal intrusion front.

3.1. Bubbles

Bubbles are injected into the ocean by breaking waves. In the presence of downwelling currents these bubbles can be subducted to depths greater than those associated with breaking waves alone ([Thorpe, 1982](#); [Baschek et al., 2006](#)). At their resonance frequencies, bubbles have scattering cross-sections much larger than their geometric cross-section, making even low bubble densities acoustically significant. The resonance frequency [kHz] of bubbles in water can be approximated by

$$f_R \approx \frac{3.25 \cdot 10^6 \sqrt{(1 + 0.1z)}}{a}, \quad (1)$$

where a is the bubble radius [μm] and z is the depth [m] ([Medwin, 1977a](#); [Medwin and Clay, 1998](#)). Prior observations of acoustic resonance from bubbles in the upper ocean show f_R spans a broad range of frequencies from ~ 10 kHz to 100 s of kHz ([Medwin, 1970](#); [Breitz and Medwin, 1989](#); [Vagle and Farmer, 1992](#); [Dahl and Jessup, 1995](#); [Terrill and Melville, 2000](#)).

Linking the bubble size distribution to acoustic backscatter requires a formulation for the backscattering cross-section, σ_{bs} , of bubbles as a function of frequency. The term σ_{bs} has units of area and is widely used to quantify single scatterers. [Vagle and Farmer \(1992\)](#), and references therein) provide the following relationship for a spherical, air-filled bubble:

$$\sigma_{bs}(f) = \frac{4\pi a^2}{\left[\left(\frac{f}{f_R}\right)^2 - 1\right]^2 + \delta^2}, \quad (2)$$

where δ is a damping constant depending on the properties of the gas in the bubble, the surrounding water, and the water-bubble interface ([Medwin, 1977b](#)). The total damping constant, $\delta = \delta_r + \delta_t + \delta_v$, includes damping due to re-radiation ($\delta_r = ka$), thermal conductivity ($\delta_t = D [f_R/f]^2$), and viscosity ($\delta_v = 4\mu/[2\rho\pi f a^2]$), where k is the acoustic wavenumber, ρ is the ambient water density, and μ is the shear viscosity. The term D contains additional terms including the gas density, thermal conductivity, and specific heats and can be found in numerous sources ([Devin, 1959](#); [Medwin and Clay, 1998](#)).

Total backscattering from a population of bubbles, per unit volume, is described by the volume backscattering coefficient

$$\sigma_V(f) = \int_0^\infty \frac{4\pi a^2 N(a) da}{\left[\left(\frac{f}{f_R}\right)^2 - 1\right]^2 + \delta^2}, \quad (3)$$

where $N(a)da$ is the number of bubbles per m³ per μm increment. When multiple scatterers are present within a volume, measurements of ABS are commonly reported as the volume backscattering coefficient (σ_V) in its logarithmic form $S_V = 10 \log_{10}(\sigma_V)$, where σ_V has units of inverse length. The general frequency dependence associated with Eq. (3) is ultimately dependent on the bubble size distribution and therefore varies in space and time. Although the backscattering cross section of a given bubble is highest at resonance, off-resonance scattering from larger bubbles can still approach or exceed that of smaller bubbles ([Medwin and Clay, 1998](#)). Depending on the bubble size distribution this could lead to overestimates in the total number of small bubbles if sampled frequencies do not resolve relatively large bubbles in the population at resonance. Nonetheless, [Medwin \(1977b\)](#) notes prior measurements of bubble size distributions in salt and fresh water suggest that the attribution of backscattering primarily to bubbles at or near resonance is reasonable while ([Vagle and Farmer, 1998](#)) show that the most significant impacts are likely to be observed for small bubbles (e.g., $a \lesssim 10 \mu\text{m}$). Prior observations and those discussed herein suggest that S_V is expected to decrease weakly with frequency across the expected band unless a low-frequency spectra roll-off is observed because large bubbles are not present in the population.

While there has been work focused on the bubble size distribution under breaking waves (e.g., [Deane and Stokes, 2002](#); [Trevorrow, 2003](#)) and in Langmuir cells (e.g., [Thorpe et al., 2003](#)), [Reeder et al. \(2022\)](#) is the only published work known to the authors that focuses on bubble size distributions in estuarine fronts. Bubble observations at a tidal front with strong bathymetric forcing is otherwise the closest published analog ([Baschek et al., 2006](#)).

If consistent with published data from other environments, the bubble population under breaking waves that is available for entrainment and advection by downwelling currents is described by a power law of the form $N(a) = \kappa a^\gamma$, where κ is a scaling factor that depends on the total number of bubbles and γ is the slope of the size distribution, which has negative values such that small bubbles are more numerous

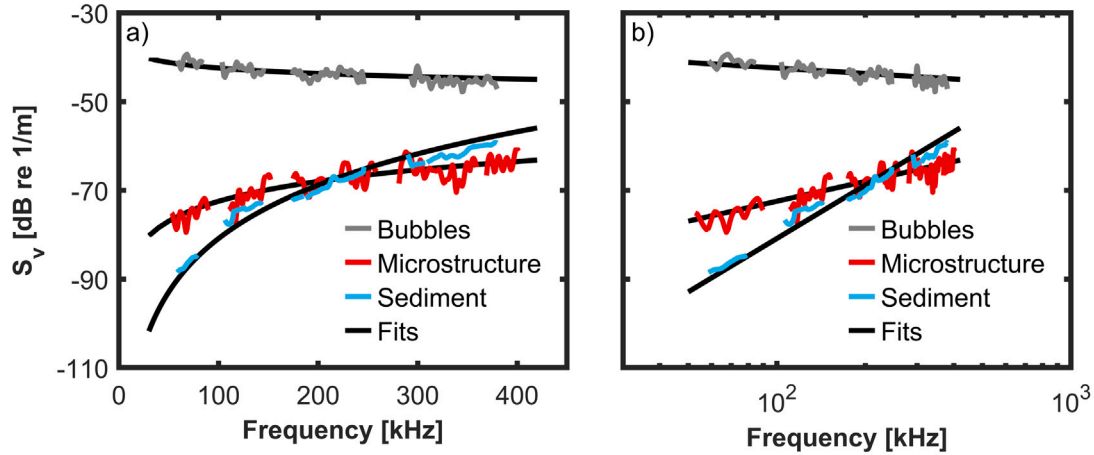


Fig. 2. Examples of backscattering from three sources presented with linear (a) and logarithmic (b) x-axes. The spectra are derived from examples shown elsewhere in this paper and the fits to the data agree well with analytical models described in Section 3.

than large bubbles (Johnson and Cooke, 1979; Vagle and Farmer, 1992; Terrill et al., 2001; Deane and Stokes, 2002; Al-Lashi et al., 2016).

The fate of a bubble entrained at the tidal intrusion front is dependent on the bubble's size, the downwelling current, and the presence of turbulence. We evaluate two limiting scenarios for the maximum bubble sizes present at depth, which are related to (1) the Hinze scale and (2) the balance between downwelling currents and bubble rise velocities. The Hinze scale describes the largest bubbles that are not fragmented by turbulence under breaking waves (Deane and Stokes, 2002). Bubbles injected in the presence of downwelling currents will be subducted if drag forces are sufficient to overcome their buoyancy-driven rise velocities. Terminal velocities for “dirty bubbles” (those affected by surface-active materials) can be estimated by

$$w_{\text{bubble}} = \frac{33a^2}{(a + 0.37)^2}, \quad (4)$$

where a is the bubble diameter [mm] and w_{bubble} has units of cm/s (Lewis and Schwartz, 2004). Inherent in the application of this formulation is the assumption that void fractions in the observed plumes are sufficiently low that the rise velocities of individual bubbles are not dependent on others.

3.2. Turbulent microstructure and interfaces

Small-scale, homogeneous, and isotropic fluctuations in temperature and salinity result in acoustic scattering. Lavery et al. (2013) provides a formulation for acoustic backscattering from stratified turbulence in the viscous-convective subrange. In environments with intense turbulence and strong vertical velocity gradients, like many estuaries, signals from this subrange can produce relatively strong signals at frequencies used by commercial echosounders (Goodman, 1990). The formulation for ABS in the viscous convective subrange is valid for wavenumbers between $k^* = 0.036k_v$ and $k_{BT,S} = (\epsilon/\nu D_{T,S}^2)^{1/4}$, where ν is the molecular viscosity, ϵ is the dissipation rate of turbulent kinetic energy, $k_v = (\epsilon/\nu^3)^{1/4}$ is the Kolmogorov wavenumber, and $k_{BT,S}$ is the Batchelor wavenumber, and the molecular diffusivities of temperature and salt are approximately $D_T = 1.5 \cdot 10^{-7}$ m²/s and $D_S = 1.5 \cdot 10^{-9}$ m²/s, respectively. The volume scattering coefficient is then described by

$$\sigma_V(k) = 2^{-3} \Psi^{ac} q \chi_S k \left(\frac{\epsilon}{\nu}\right)^{-1/2}, \quad (5)$$

where $q = 3.7$ is a dimensionless constant (Oakey, 1982), χ_S [PSU²/s] is the dissipation rate of salinity variance, and k is the acoustic wavenumber. Ψ^{ac} [PSU⁻²] contains terms relating to changes in mean temperature, mean salinity, and fractional changes of sound speed and density.

Eq. (5) indicates that the frequency-dependent volume backscattering strength for stratified turbulence in the viscous-convective subrange is expected to increase with f^1 and that it is more sensitive to the dissipation rate of salinity variance than to the dissipation rate of turbulent kinetic energy. As with bubbles, Eq. (5) is often presented in a logarithmic form, $S_V(f) = 10 \log_{10}(\sigma_V(f))$.

To invert ABS data for χ_S or ϵ , it is necessary to estimate Ψ^{ac} from CTD measurements and apply local relationships between temperature and salinity. Furthermore, the backscattering cross-section in the viscous-convective subrange depends on the product of two unknown parameters, $\chi_S \epsilon^{-1/2}$. Dissipation flux estimates (Moum, 1996), sometimes referred to as mixing efficiencies, are related to the flux Richardson number which can be approximated as, $R_f \approx g\beta\chi_S / [2\epsilon(\partial\bar{S}/\partial z)]$, where g is the acceleration due to gravity and $\beta = \frac{1}{\rho} \frac{\partial\rho}{\partial S}$, can be used to relate ϵ and χ_S (Gargett and Moum, 1995; Thorpe, 2007; Gregg et al., 2018). Use of the flux Richardson number in Eq. (5) gives,

$$\chi_S = \left(\frac{\sigma_V}{2^{-3}\Psi^{ac}qk}\right)^2 \left(\frac{g\beta}{2R_f}\right) \left(\frac{\partial\bar{S}}{\partial z}\right)^{-1} \nu^{-1}, \quad (6)$$

and

$$\epsilon = \left(\frac{\sigma_V}{2^{-3}\Psi^{ac}qk}\right)^2 \left(\frac{g\beta}{2R_f}\right)^2 \left(\frac{\partial\bar{S}}{\partial z}\right)^{-2} \nu^{-1}. \quad (7)$$

This formulation is applicable for the observations presented here, which supporting measurements and analysis suggest fall within the viscous-convective subrange. Lavery et al. (2003) provides similar formulations for wavenumbers in the inertial-convective subrange.

The gradient Richardson (Ri) number is a non-dimensional number relating the density gradient to vertical shear in stratified flows. Its value provides an indication of stability and is used to identify areas with expected turbulent mixing (e.g., shear instabilities) and those where stratification is stable at the scales resolved by in situ physical measurements. Ri is defined as

$$\text{Ri} = \frac{-g \frac{d\rho}{\rho dz}}{\left(\frac{du}{dz}\right)^2}, \quad (8)$$

where u is the horizontal velocity. Localized shear instabilities and overturning are expected when $\text{Ri} < 0.25$. Here, the prior formulations for scattering from turbulent microstructure are applied to areas where active mixing from shear instabilities is observed. Many prior studies including Haury et al. (1979), Farmer and Dungan Smith (1980), Geyer et al. (2010), Lavery et al. (2013) and Holleman et al. (2016) show examples of similar high-resolution imaging of instabilities using echosounders.

Where $Ri > 0.25$, stratification is considered stable at the scale of the measurements. In these circumstances, acoustic backscattering is driven by gradients in the acoustic impedance ($Z = \rho c$, where c is the sound speed). Throughout this manuscript the word *interface* is used to describe relatively thin (i.e., <10 cm) layers of elevated ABS corresponding to these sharp gradients. This language is chosen to differentiate these regions from scattering associated with active mixing or density overturns, which typically appear as either coherent structures associated with hydrodynamic instabilities or as more diffuse layers associated with larger vertical scales.

Scattering from such interfaces has been considered in many studies (Fisher and Squier, 1975; Penrose and Beer, 1981; Lavery and Ross, 2007; Ross and Lavery, 2011; Stranne et al., 2017, 2018; Weidner et al., 2020; Weidner and Weber, 2021). Nonetheless, interpretation of these signals requires a broad range of assumptions related to interface roughness, range dependence, and property gradients, which affect frequency-dependent scattering. Assuming an acoustically smooth interface, the amplitude reflection coefficient for a plane wave at normal incidence is described by

$$R = \frac{(Z_2 - Z_1)}{(Z_2 + Z_1)}, \quad (9)$$

where Z_1 and Z_2 are the acoustic impedance values for the water at two adjacent depth bins in the profiles. This formulation assumes a step function between the properties at the two depths and thus does not capture the combined impact of gradients and acoustic wavelengths. The presentation of relevant acoustic results here is limited to comparisons between S_V and areas with elevated intensity reflection coefficients (R^2) corresponding to measured property gradients. Quantitative interpretations of ABS from interfaces is beyond the scope of this manuscript but is discussed further in Section 5.

3.3. Suspended sediment

Transport of sediments by resuspension and advection occurs when shear stresses on the seabed rise to sufficiently high levels that the lift forces imposed on sediments overcome their negative buoyancy. Particles are therefore dislodged from the seabed and transported with local currents. The nature of sediment transport is predicted by the non-dimensional Rouse number, \mathcal{P} (Rouse, 1939; Whipple, 2004):

$$\mathcal{P} = \frac{w_s}{\kappa u_*}, \quad (10)$$

where w_s is a particle's settling velocity, $\kappa = 0.41$ is the von Karman constant, and u_* is the shear velocity. An additional constant relating eddy viscosity and eddy diffusivity is sometimes included in Eq. (10), but is neglected here as it is assumed to be approximately equal to 1. Bedload is the dominant transport mechanism when $\mathcal{P} > 2.5$, whereas sediments are suspended to varying degrees for $\mathcal{P} < 2.5$. For $\mathcal{P} < 1.2$ the sediment load is dominated by suspended sediment.

The settling velocity, assuming a small spherical particle, is calculated according to Stokes' Law:

$$w_s = \frac{(\rho_s - \rho_w)}{18\mu} g D^2, \quad (11)$$

where D is the particle diameter, μ is the dynamic viscosity, ρ is the density, and the subscripts s and w refer to the sediment and water, respectively. For relatively large or dense particles the Reynolds number exceeds those where Stokes' Law is valid and settling velocities are lower than those predicted by Eq. (11). Therefore, alternative formulations such as those presented by Dietrich (1982) are required and can accommodate factors such as the grain's shape.

Sediment cores from locations in the vicinity of the acoustic analysis here were dominated by fine to medium sands ($200 \mu\text{m} < D_{50} < 300 \mu\text{m}$) and shell hash. Smaller amounts of silt and course-grained sediments up to a few mm were also encountered at these sites. Upriver and well outside of the region of the tidal intrusion front,

seabed samples were dominated by fine-grained, cohesive sediments. These sediments, such as clays and silts, tend to flocculate (to form "flocs") forming large-diameter, low-density, porous aggregations of much smaller sediments. Perkey et al. (2020) performed experiments using optical cameras to observe flocs eroded from cores taken in the lower James River. The samples were taken several kilometers upriver from the tidal intrusion front, but are likely to be representative of the fine sediment characteristics in the lower estuary. Eroded flocs from the cores had size distributions with D_{50} values of $270 \mu\text{m}$ and $380 \mu\text{m}$, respectively. Properties of flocs from Perkey et al. (2020) and sands sampled at the site are used to constrain properties for ABS scattering models.

For sand measured at the site estimated settling velocities calculated according to Dietrich (1982) range from approximately 20 to 35 mm/s assuming a particle density of 2650 kg/m^3 , a Corey shape factor of 0.7, and Powers roundness factor of 3.5. To calculate Rouse numbers a shear velocity is necessary and can be estimated using according to $u_*^2 = C_d u_{bot}^2$, where u_{bot} is the near-bed velocity. We assume a drag coefficient of $C_d = 3 \cdot 10^{-3}$ and use peak velocities of 0.90 m/s that were measured by the moored ADCP 1.7 m above the seabed to calculate peak u_* values of approximately 0.05 m/s. Representative Rouse number estimates corresponding to the currents during acoustic sampling and the range of sand grains measured at the site are $\mathcal{P} \sim 1.3$ to $\mathcal{P} \sim 2.2$. These values indicate the possibility of suspended loads. Given their similar size but lower density, Rouse numbers corresponding to flocs are considerable lower than those associated with sands. Flocs would therefore be expected to be present in higher concentrations than sands well above the seabed.

Bedload transport and high near-bed concentrations cannot be effectively measured using the acoustic backscattering techniques discussed here due to the proximity to the seabed and strong sidelobes of the seabed echo (Lavery et al., 2017). Thus, our focus is on suspended sediment. Given the Rouse numbers, our analysis allows for the possibility of suspended sand grains or the resuspension of flocs that may have settled during a prior slack tide.

Acoustic scattering models for suspended sediment often assume that the particle is well-represented by a sphere with an equivalent volume. Further simplifications to scattering models, which are valid for fluid or solid scatterers, can be achieved if suspended sediments are in the Rayleigh scattering regime ($ka \ll 1$). Assuming a maximum diameter of $380 \mu\text{m}$, $ka < 0.33$ across the sampled bandwidth. Thus, we model the backscattering cross-section as a sphere in the Rayleigh scattering regime, which is described by

$$\sigma_{bs} = k^4 a^6 \left[\frac{1 - g_s h_s^2}{3g_s h_s^2} + \frac{1 - g_s}{1 + 2g_s} \right]^2, \quad (12)$$

where a_s is the radius of the sediment grain (or floc), $g_s = \rho_s / \rho_w$ is the ratio of the densities, and $h_s = c_s / c_w$ is the ratio of the sound speeds (Rayleigh, 1945; Anderson, 1950; Johnson, 1977). This formulation shows that an f^4 frequency is expected for the size of suspended sediments and frequencies considered in this study. Model outputs for σ_{bs} here are presented as the target strength where $TS = 10 \log_{10}(\sigma_{bs})$. For an arbitrary distribution of suspended sediments, Eq. (12) is modified such that

$$\overline{\sigma_{bs}} = \sum_{i=1}^m \sigma_{bs}(a_i) P(a_i), \quad (13)$$

where $\overline{\sigma_{bs}}$ is the mean backscattering cross section, $P(a_i)$ is the probability associated with sediments with radius a , and i is an index corresponding to a given radius in the distribution.

The appropriate material properties for Eq. (12) are dependent on the type of suspended sediment being observed. For scattering attributed to a distribution of sand grains $\rho_s = 2650 \text{ kg/m}^3$ and $c_s = 5800 \text{ m/s}$ are appropriate (MacDonald et al., 2013). In contrast, flocs are porous and have bulk densities and sound speeds more similar to the surrounding water. Using a representative bulk density for resuspended

flocs of $\rho_f = 1300 \text{ kg/m}^3$ (Perkey et al., 2020), the porosity of flocs is described by

$$\phi = \frac{(\rho_s - \rho_f)}{(\rho_s - \rho_w)}, \quad (14)$$

where $\rho_s = 2650 \text{ kg/m}^3$, $\rho_w = 1011 \text{ kg/m}^3$, and the subscript f refers to the floc. The bulk sound speed for a floc is determined according to Wood's equation (Wood, 1930) such that

$$\frac{1}{c_f^2} = [(1 - \phi)\rho_w + \phi\rho_s] [(1 - \phi)\kappa_w + \phi\kappa_s], \quad (15)$$

where κ_s and κ_w are the respective compressibilities ($1/\rho c^2$) of the sediment and water. Eqs. (12)–(15) are then used to model the backscattering cross section. More complex, hybrid formulations combining elastic scattering from the individual, small-grained constituents with the fluid-like scattering from flocs have been published (e.g., Thorne et al., 2014). However, the results discussed herein fall in the ka regime where Thorne et al. (2014) suggest the flocs behave largely as fluid scatterers. Thus, we assume the medium is a fluid and therefore cannot support shear waves.

The modeled backscattering cross section and the measured volume backscattering coefficient can be used to estimate the numerical density of particles according to

$$n = \sigma_V / \overline{\sigma_{bs}}, \quad (16)$$

where $n = \int_0^\infty N(a) da$ and $N(a)$ is the number of particles per unit volume per radius. Suspended sediment concentration (SSC) in mg/L is then estimated by

$$SSC = 1000n \sum_{i=1}^m \frac{4}{3} \pi a_i^3 P(a_i) \rho_{sed}, \quad (17)$$

where the right-hand side of the equation represents the mean density associated with $\overline{\sigma_{bs}}$ and ρ_{sed} is the density of the sediment (i.e., ρ_s or ρ_f). Local measurements of optical backscatter (OBS) in nephelometric turbidity units [NTU] are compared to acoustically inferred suspended sediment concentrations.

NTU is a relative unit and requires calibration against suspended particulate concentration. Measured optical backscattering is strongly affected by changes in size, shape, and material composition of suspended sediments (Downing, 2006). However, if these properties are relatively constant over the duration of an experiment a linear relationship between SSC and turbidity (in NTU) is expected to have a slope between 0.5–2 (Guillén et al., 2000; Downing, 2006). Here, no such calibrations are available so we assume that, given the short timescale and highly localized nature of the experiment, these parameters do not vary considerably. Data from numerous locations in the York River, an adjacent estuary in the Chesapeake Bay, fitted for SSC versus NTU, had slopes that varied between 1–2 (personal communication, Carl Friedrichs based on the data in Fall (2020)). Based on these considerations we assume that the slope relating SSC to NTU is between 0.5–2 to investigate acoustically inferred suspended sediment concentration as described above.

3.4. Acoustic data processing

The EK80 transceivers used for ABS measurements record complex-valued time series values for each ping. Using header information, each ping is pulse-compressed and stored for further processing. All acoustic channels were calibrated following the experiment using on-axis calibration techniques (Demer et al., 2015) with 21.2 mm and 38.1 mm tungsten carbide spheres with 6% cobalt binder. In post-processing, transducer performance issues associated with individual transducer quadrants having impedance values varying from those expected were observed on the 70 kHz and 120 kHz units. These impedance values alter the transmit and receive mode performance and were determined to be different between James River and the post-experiment calibration

data. Therefore, post-experiment calibration gains could not be directly applied to the 70 kHz and 120 kHz channels.

An additional heuristic “correction” approach was therefore applied. To do this, scattering from the seabed, turbulent microstructure, and suspended sediment and the analytical models describing the frequency dependencies, were used to align the data with the 200 kHz and 333 kHz channels for which suitable calibration curves existed. Further information about this heuristic correction is included as supplemental material. The gains from the heuristic correction from the 70 and 120 kHz channels are applied to all volume scattering measurements with these transducers but precluded their use in the analysis of individual targets. Using this heuristic approach, ABS observations are consistent with a priori expectations informed by scattering models but nonetheless have a higher degree of uncertainty than typical, calibrated measurements.

ABS measurements are presented in three different forms throughout this manuscript and data products were calculated using the power budget equations described in Demer et al. (2017). First, echograms present measured volume backscattering coefficients in their logarithmic form $S_V(t)$ [dB re 1/m], as a function of depth and along-channel coordinates. The notation $S_V(t)$ is chosen to differentiate the presentation of pulse-compressed signals, which are converted to range using the sound speed, from the presentation of volume scattering as a function of frequency. Second, frequency spectra from volume backscattering, $S_V(f)$ [dB re 1/m], are presented for measurements of bubbles, microstructure, and suspended sediment. The final form, target strength, $TS(f)$ [dB re 1 m²] is applied only to biological targets and is summarized in the supplemental material.

Spectra were calculated for the different sources of backscattering by averaging over scales consistent with their spatial scales. All backscattering spectra attributed to specific sources were calculated by processing specific ping indices and depth ranges corresponding to the images obtained from $S_V(t)$. Data were zero-padded and transformed using 2¹² points, window lengths of 0.4 m with 10% Tukey windows, and overlaps of 50%. Presentations of scattering attributed to a source and location were then averaged following a manual review to exclude noise spikes attributed to acoustic cross-talk associated with other systems deployed from the vessel (e.g., the ADCP) or elsewhere in the estuary.

Data were also processed to calculate the spatial distribution of spectral slope as a proxy for the dominant source of backscattering (Section 3, Fig. 2). To produce this data product the 70 kHz, 120 kHz, and 200 kHz channels were used. The 333 kHz channel was not used due to its higher noise floor from persistent electrical noise. Throughout the water column S_V spectra were calculated using 0.3 m windows with 50% overlap, and 10% tapered Tukey windows. For each window a linear regression of $S_V(f)$ versus $10 \log_{10}(f)$ was calculated. The slopes of these lines, ranging from roughly –2 to 4, captured the range of expected spectral slopes for the sources of ABS. Spectral slope results were smoothed by applying a uniformly weighted spatial average covering three adjacent pings (~2 m in the horizontal) and three vertical windows spanning approximately 0.6 m.

Integrated volume backscattering was calculated to compare bubble-driven ABS in the upper water column with air-side remote sensing of frontal features. For each ping, the volume backscattering time series was integrated for ranges 2–5 m from the transducer using the 70 kHz transducer. Values were then smoothed using a three-ping moving average. This integrated acoustic backscattering is plotted in the linear domain and mapped against radar observations of front locations to reveal increases in near-surface scattering from bubbles.

3.5. Forward and inverse modeling

Different methods for inverse and forward modeling are applied to different inferred sources of volume backscattering. The data inputs to

all forward and inverse models are the linear form of the $S_V(f)$ spectra processed using the methods described in Section 3.4.

Bubbles: Volume backscattering from a bubble population is described by Eq. (3). To avoid an ill-conditioned system of equations we adopted an iterative technique motivated by Caruthers et al. (1999) with modifications to estimate bubble size distributions. This method applies the resonant bubble approximation, which assumes that only bubbles resonant at a given frequency contribute to backscattering. For each inversion, the ABS spectrum was fit using a second-order polynomial to smooth the noise inherent in acoustic spectra (Fig. 3). From this fit the initial inversion for the bubble size distribution (N_i) is made using the resonant bubble approximation. N_i is then applied to numerically evaluate the Fredholm integral (Eq. (3)) yielding $S_{v,fr}(f)$. After each step we calculate the mean-square error of $S_{v,meas} - S_{v,fr}$, where $S_{v,meas}$ is the measured spectra and $S_{v,fr} = 10 \log_{10}(S_{v,fr})$. If the mean-square error exceeds 0.5 dB a new bubble size distribution is estimated according to:

$$N_{i+1, rba} = N_{i, rba} - (N_{i, rba} - N_{i, fr})/10, \quad (18)$$

where subscript $_{rba}$ denotes distributions associated with the resonant bubble approximation, $_{fr}$ with the Fredholm integral, and indices i and $i + 1$ for the current, and next iterations, respectively. For each iteration $N_{i, fr}$ represents the new distribution of bubbles calculated using the resonant bubble approximation with the modeled ABS from the Fredholm integral. Bubble distributions resulting in mean-square error values less than 0.5 dB were determined to have converged and are reported along with the forward modeled results from Eq. (3).

Turbulent microstructure: Inversions for the dissipation rates of turbulent kinetic energy and salinity variances were performed in a two-step process. First, spectral fits ($\log_{10}(f)$ versus $S_V(f)$) were used to identify areas with frequency responses consistent with microstructure (i.e., slopes $< f^{0.5}$ or $> f^2$ were removed from the analysis). Given that individual spectra are noisy, mean $S_{V(f)}$ curves were calculated in uniformly weighted 3×3 , moving windows. Next, spectral fits were produced by first smoothing (10 points) the mean spectra and performing a polynomial fit to the curve based on the spectral slope. The value of the curve fit to mean $S_{V(f)}$ curve at 280 kHz was then selected for the inversion. We note this frequency was arbitrary, which is not problematic as long as the assumptions inherent in the scattering model apply over the frequency ranges to which the fit was performed. Mean salinity gradients were calculated from the microstructure profiler and towed-array measurements. On 21 April 2019 this yielded $\frac{\partial S}{\partial z} = 0.8$ PSU/m. Combined temperature and salinity measurements around the

salt wedge on 21 April yielded a mean slope of approximately $\frac{\partial T}{\partial S} = 0.2^\circ\text{C}/\text{PSU}$ with Ψ^{ac} values of $\approx 3.7 \cdot 10^{-6}$ PSU $^{-2}$. A mixing efficiency of 0.2 (Holleman et al., 2016) was assumed for the inversions. Turbulent parameters including ϵ and χ_s are plotted and compared to estimates from in situ measurements.

Interfaces: For comparison to backscattering, CTD profiles with 10 cm resolution were used to calculate the sound speed (Chen and Millero, 1977) and density (Millero et al., 1980). The amplitude reflection coefficient was then calculated from the profiles according to Eq. (9), which is squared and presented as the intensity reflection coefficient. These profiles are presented alongside echograms of volume backscattering to demonstrate qualitative agreement between in situ measurements and ABS.

Suspended sediment: Inversions for suspended sediment concentrations rely on the application of models for a given sediment size or distribution. However, in this study the scattering was assumed to be entirely within the Rayleigh scattering regime and the parameter space that could converge to a solution was not well-constrained. Based on literature and sediment cores we modeled solutions with the properties of sand grains and flocs (Section 3.3). Next, backscattering spectra from areas where the spectra slope was consistent with scattering from suspended sediment (f^4 in the Rayleigh scattering regime) were selected and the average volume backscattering coefficient was calculated from 330–355 kHz. This range was chosen because the signal from suspended sediment is strongest at higher frequencies and narrowband electrical noise was negligible within this band. Eqs. (16)–(17) were then used to infer suspended sediment concentrations given different sediment sizes and distributions. Models for suspended flocs and sand grains are used to make comparisons between modeled SSCs and turbidity measurements.

4. Results

Acoustic backscattering measurements from 20–25 April 2019 exhibit consistent periodicity due to the tidal forcing that decreased throughout the experiment during the transition from spring to neap tides. During flood tides, a v-shaped tidal intrusion front forms and extends westward from the Monitor–Merrimac Memorial Bridge–Tunnel (Fig. 4). A salt wedge propagates below the buoyant river discharge upriver from the front. The point where the salinity interface meets the surface is the tidal intrusion front’s surface expression. It is the site of intense surface convergence, elevated acoustic backscattering throughout the upper half of the water column (~ 10 m), and elevated surface roughness along the front as measured by the radar (Fig. 5). The ADCP and towed CTD measurements show that the frontal interface is narrow.

SWIFT drifter measurements and the ADCP measurements from the mooring (Fig. 6) show good agreement, with maximum downwelling velocities between 10–20 cm/s, which is consistent with prior observations at the site (Marmorino and Trump, 1996). Mean downwelling velocities peak between 3–7 m below the surface. We note that ADCP velocity measurements assume passive tracers, and the rise velocities of the bubble may bias these measurements towards lower values. Measurements as the front passes over the mooring show a short period (≈ 10 s) associated with the strongest downwelling, while the full signal propagates past the mooring in about 70 s.

Early in the experiment, when tides are stronger, the intrusion front extends further westward. The position of the intrusion front also responds to surface wind forcing. Winds from the north (25 April) tend to favor southwesterly surface currents during the flood tide, while winds from the south (21 April) result in more westerly directed surface currents (Fig. 5). These patterns are also captured by the circulation model. Variations in tidal mixing also exert an important control on vertical density stratification. The decrease in tidal mixing that occurred during the experiment resulted in an intruding water column that was increasingly stratified, with ABS data showing a number of interfaces.

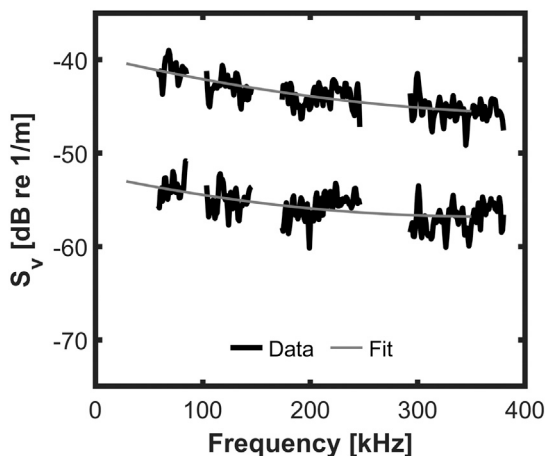


Fig. 3. Two examples of ABS associated with bubble plumes. The fits show the second-order polynomial fits used in the inversions for bubble size.

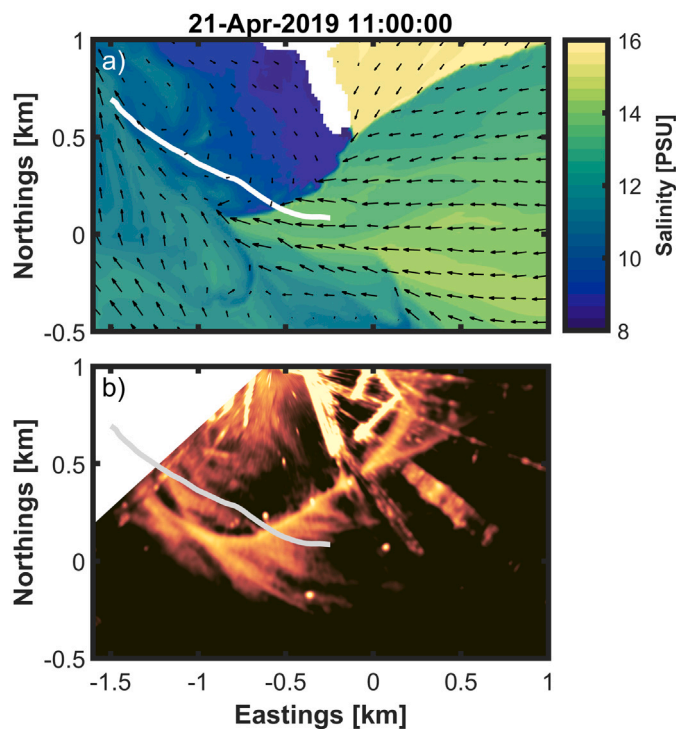


Fig. 4. (a) ROMS model output and (b) a radar image for 11:00 on 21 April, a period when the tidal intrusion front is arrested and exhibits a notable “v” shape. Vectors of surface velocity in (a) show strong convergence at the front where salinity gradients are relatively strong. Stronger radar backscatter (denoted by brighter colors) near the front is associated with greater surface roughness where velocity convergence causes surface waves to steepen. Each figure shows a vessel transect (gray line) corresponding to the same time period, which is used in other examples throughout this paper.

Scattering from near-bottom suspended sediments was greater early in the experiment when OBS measurements showed the highest levels of near-bed turbidity.

While physical oceanographic measurements and model simulations provide some insight into the dominant scattering mechanisms, ABS spectra provide a quantitative approach to inferring which mechanisms dominate the observed scattering. Given the strong convergence, current velocities and gradients, and salinity structure in the vicinity of the front, the ABS is highly variable. An echogram and the corresponding spectral slopes for a single along-channel transect (Fig. 7) demonstrate this variability. The following sections provide details about the ABS observations of bubble plumes, turbulent microstructure and interfaces, suspended sediment, and biological backscattering (supplemental material), which can be directly related to the observed spectral structure.

4.1. Bubbles

The highest intensity ABS measurements in the James River were associated with bubbles near the surface expression of the tidal intrusion front. Here we identify the spatial distribution of ABS attributed to bubbles but do not assess the kinematics of the observed bubble plumes in detail. ABS from bubbles is easily distinguished from other sources because it is relatively intense at frequencies below 100 kHz and the scattering spectra for entrained bubble distributions have flat or negative slopes. In general, bubble plumes reach depths between 7–12 m, or about one-third to one-half of the water column, with the most intense scattering observed within 10 m of the front. Subducted bubbles are advected landward along the pycnocline, with ABS from bubbles often extending 100–200 m from the front. Landward from the

front the ABS signals from the subducted bubble plumes do not extend to the surface, suggesting that the bubbles more than 50 m upriver are relatively small and insufficiently buoyant to rise to the surface during the timescales of advection from the front. These descriptions of the plume structure are consistent with prior observations of the James River tidal intrusion front, which describe spatial scales for frontal convergence and bubble entrainment on the order of 6 m (Marmorino and Trump, 1996).

Acoustic inversions for bubble size distributions (Fig. 8) are limited to approximately $10 \mu\text{m} < a < 100 \mu\text{m}$ due to the sampled bandwidth. The slopes of the inferred bubble populations ($\sim a^{-2.3}$) are consistent with measurements below breaking waves for sizes smaller than the Hinze scale at the beginning of the quiescent phase of breaking (Deane and Stokes, 2002). Both the observed spectral slopes and those of the associated bubble size distributions were relatively consistent regardless of their proximity to the front. Similarities in plume structure and ABS intensities between transects suggest wave breaking and bubble entrainment at the front are nearly continuous processes. ABS measurements do not suggest increasingly steep spectral slopes over time, unlike the discussion in Deane and Stokes (2002). We hypothesize that this distinction is driven not only by a lack of resolution of larger bubble sizes but by the downwelling at the tidal intrusion front that creates the bubble plume despite the relatively small size of the surface waves (e.g., significant wave heights on 21 and 25 April, as measured by SWIFTS, were much less than 0.5 m). While there is consistency in the slopes of the size distributions of the inferred bubble populations, there are notable decreases in inferred densities farther from the front. These decreases in bubble densities thus correspond to either bubble escape from the plume due to buoyancy or dissolution.

The dynamic range of ABS attributed to bubbles exceeds 30 dB with the highest levels occurring in a narrow (~ 5 m) window at the plume front (Fig. 8). Within this window, evidence of multiple scattering, including a tail extending below the bubble plume and excess attenuation in the 70 and 120 kHz channels, is observed (Fig. 7). These observations suggest high bubble densities in the “near field” of the front. We hypothesize this is driven by bubbles high enough in the water column that only a portion of them are ultimately entrained and advected with the currents. Farther from the front ABS attributable to bubbles decreases until backscattering from turbulent microstructure along the salt wedge interface masks the signal. A few observations (not shown) exhibited spectral roll-off at low frequencies that are attributed to a lack of resonant bubbles. This implies that distributions throughout the plumes generally included bubbles larger than $a \approx 85 \mu\text{m}$ before masking from other sources or noise limits the ability to resolve them.

Measurements of downwelling and turbulence at the tidal intrusion front support the acoustically inferred presence of bubbles and can further constrain the dynamics driving the observed backscattering. The highly localized downwelling signals (Fig. 6) are consistent with the echograms and suggest that bubble entrainment occurs on relatively small spatial scales (< 10 m). Thus, the observed plume geometry can only be explained by the landward advection of bubbles. Using ACDP data, estimates for advective timescales for bubbles observed in the plume can be calculated from velocity profiles. Fig. 5 shows that within the bubble plume landward velocities are generally less than ~ 0.5 m/s. Therefore, bubbles remaining in the water column 100 m from the front were likely entrained at least 200 s earlier.

The localized bubble source and the sustained downwelling at the front may also affect observed plume geometries by controlling entrained bubble sizes. Based on rise velocities for dirty bubbles (Eq. (4)), peak downwelling velocities would be sufficient to entrain those with $a \approx 800 \mu\text{m}$ or less. More representative downwelling velocities on the order of 5–10 cm/s are observed deeper in the water column and farther from the front and only support the subduction of smaller bubbles (e.g., $a \approx 250 \mu\text{m}$ or less for $w = 5$ cm/s). Near-surface dissipation rates of turbulent kinetic energy from 10^{-4} to 10^{-2} W/kg, as measured by the SWIFT drifters, are representative throughout the experiment. These

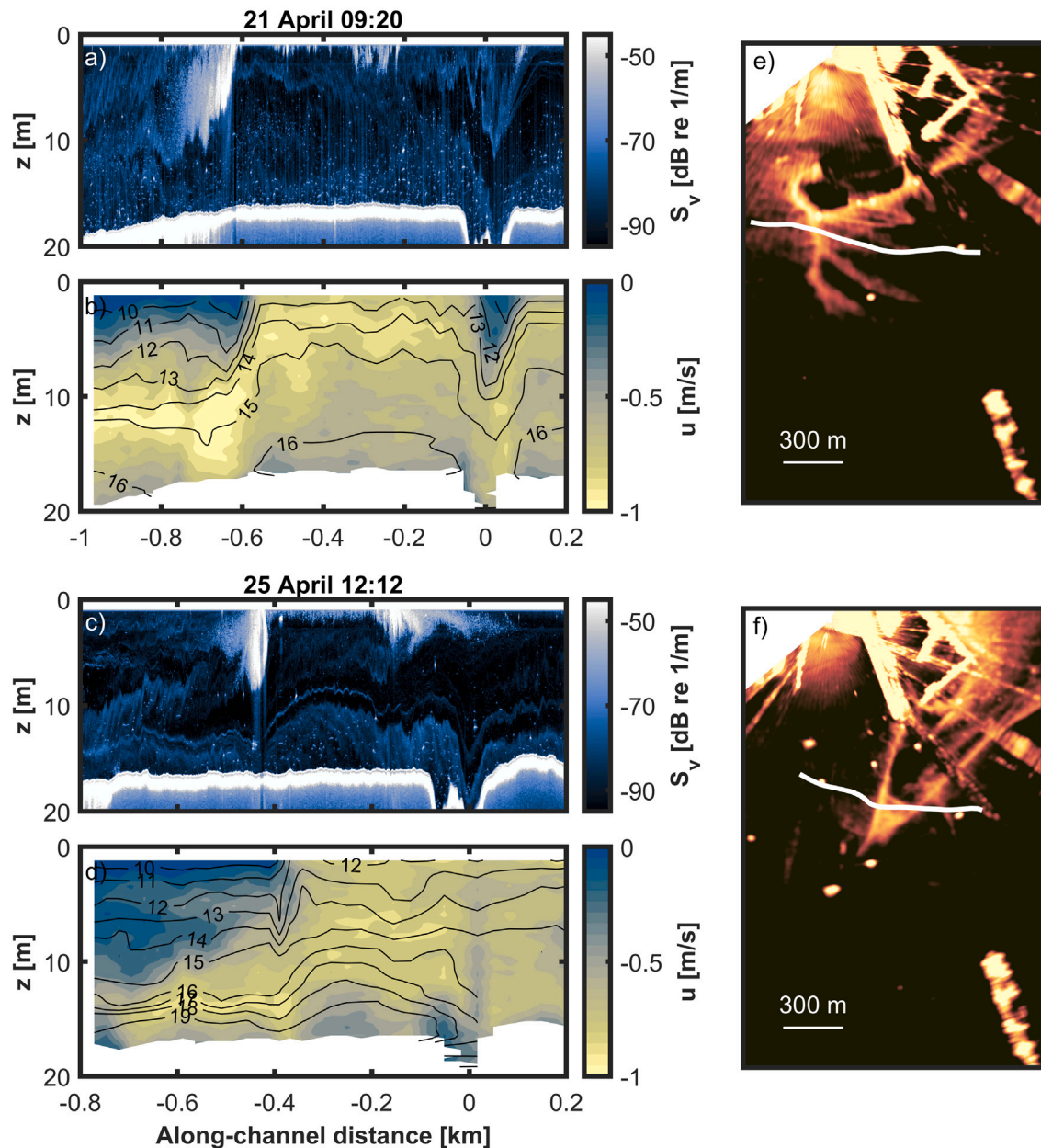


Fig. 5. Measurements corresponding to two transects at roughly the same stage of the tide on 21 and 25 April while the tidal intrusion front is propagating westward. (a,c) Acoustic backscattering (70 kHz). (b,d) E-W current velocity overlaid with salinity contours. Negative velocities correspond to westward flow. (e,f) Radar images overlaid with the portion of the vessel transects associated with the data in (a–d). The dominant features in the echograms are large bubble plumes corresponding to frontal crossings. Additional scattering from microstructure is observed elsewhere in the water column. Radar images show enhanced backscattering (brighter colors) from surface roughness at the front.

dissipation rates suggest that the Hinze scales of bubbles produced by breaking waves are larger than the sizes of bubbles likely to be entrained by downwelling. Both the Hinze scale and downwelling velocities suggest that bubbles with radii on the order of 1 mm may be present in the plume near the front. However, ADCP data suggest that bubbles with radii exceeding 300 μm ($w_{\text{bubble}} > 7 \text{ cm/s}$) would reach the surface within 10 s of meters from the front while those smaller than approximately 150 μm ($w_{\text{bubble}} < 2.5 \text{ cm/s}$) rise slowly enough that they remain meters below the surface in excess of 100 m from the front. This latter result is consistent with estimates of advective timescales. Therefore, the downwelling, not the surface breaking dynamics and turbulence, likely limits the size distribution of bubbles observed at depth as noted by Thorpe et al. (2003) with reference to Langmuir circulation.

The prior paragraphs focus strictly on the tidal intrusion front, but other fronts that entrained bubbles and increased near-surface ABS were also observed. Surface expressions of these features were confirmed in X-band radar data and physical oceanographic measurements and are present in the circulation model (Fig. 4). An additional front seaward of the v-shaped tidal intrusion front (Fig. 9) is responsible for the bubble plume over the tunnel in Fig. 7. Note that Figs. 7 and 9 are not derived from co-temporal measurements. While often present in ABS measurements in the vicinity of the tunnel, this plume instead corresponds to a secondary frontal feature, referred to here as a shear front. Circulation models and measurements show that this shear front is associated with weaker salinity gradients, yet it still results in strong ABS signals attributed to bubbles. Simpson (2021) includes numerous additional radar and sUAS images of frontal features from the experiment that were associated with these ABS signatures.

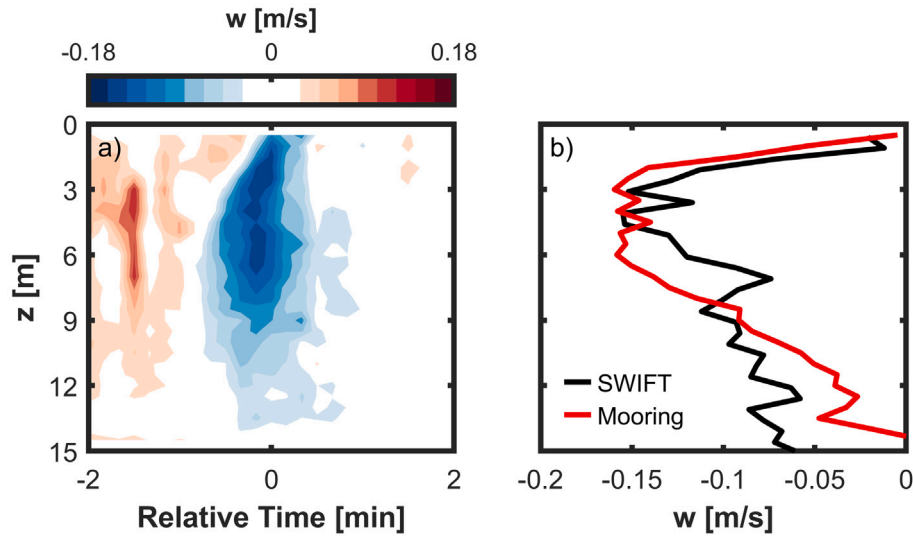


Fig. 6. (a) Vertical velocity measurements from the moored ADCP. (b) Vertical velocity profiles from the moored ADCP (10 s average at the peak in [a]) and a SWIFT drifter (60 s average) corresponding to the passage of the tidal intrusion front over the mooring on the morning of 21 April. The SWIFT was trapped in the front ~150 m SSW of the mooring at this time.

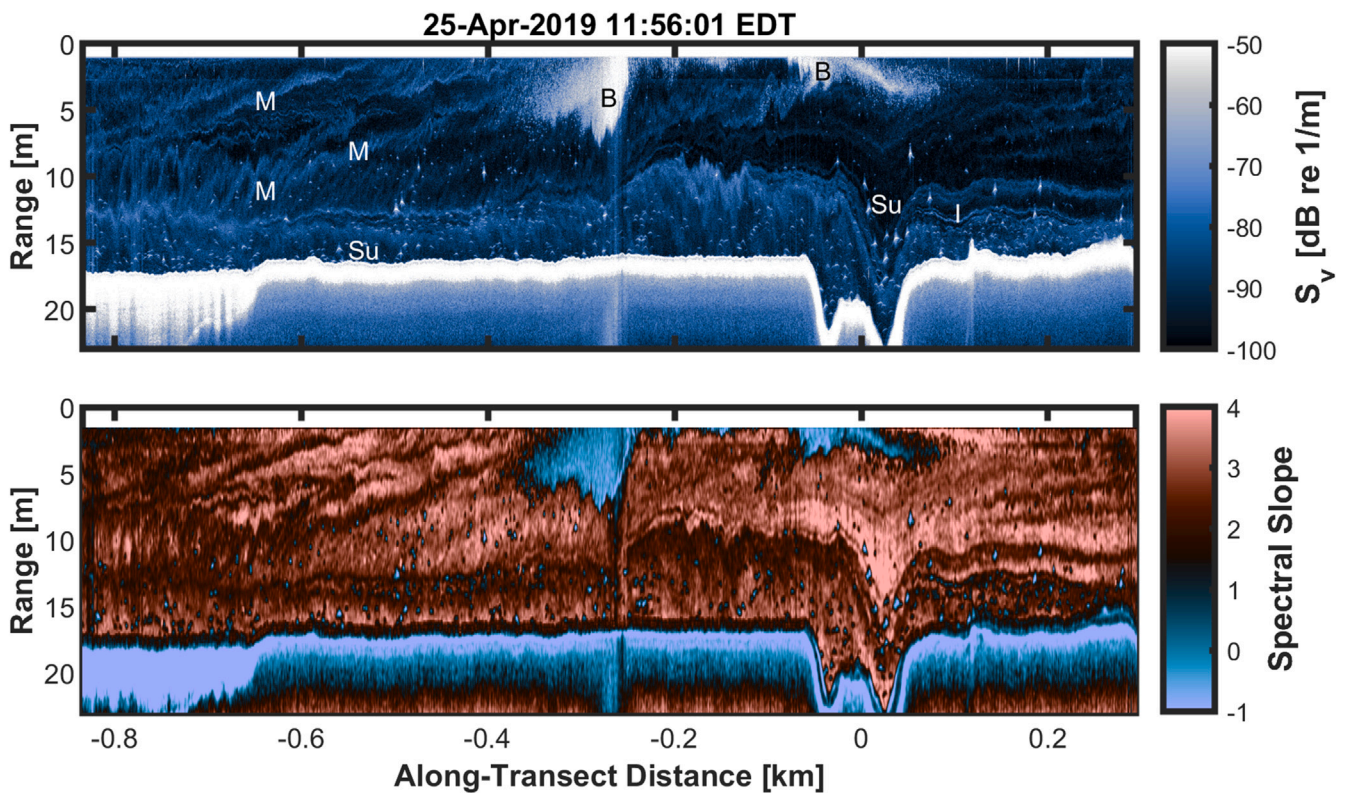


Fig. 7. (a) An echogram (70 kHz) with labeled examples of the backscattering processes and (b) spectral slopes for an along-channel transect. The colors in (b) map to the different processes such that red, black, and blue correspond to scattering from suspended sediment (Su), turbulent microstructure (M) and interfaces (I), and bubbles (B), respectively. Small areas of unlabeled, relatively intense ABS, are associated with fish. In both figures the impacts of excess attenuation (Bassett and Lavery, 2021) and multiple scattering (see Section 5) are visible at the tidal intrusion front below the bubble plume.

4.2. Turbulent microstructure and interfaces

Acoustic backscattering signals associated with mixing and stratification are common in estuarine environments and vary temporally and spatially due to a variety of forcing mechanisms. Early in the

experiment, the ambient Chesapeake Bay waters were weakly stratified, but stratification increased as the tides transitioned from spring to neap (Fig. 5). Most of the observed signals were associated with the intruding salt wedge early in the experiment. There, strong vertical shear results in instabilities and enhanced mixing. Later in the experiment similar

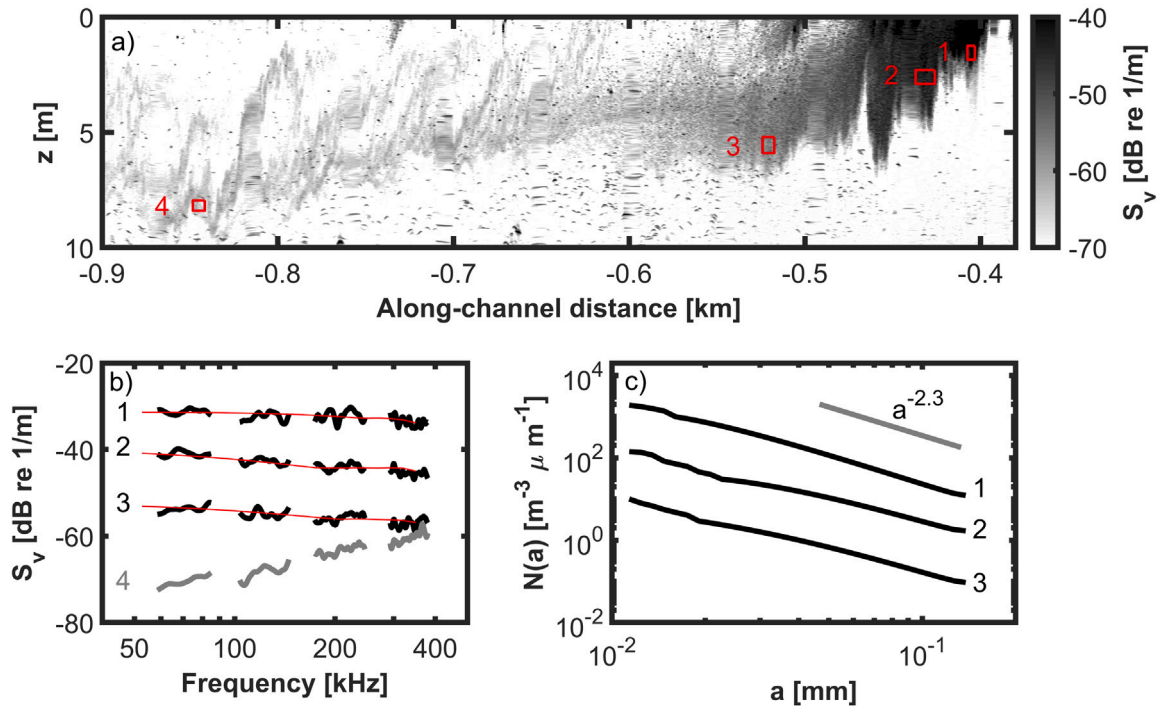


Fig. 8. (a) An echogram highlighting areas used to produce volume backscattering spectra. The numbers in other subplots correspond to these labels. (b) $S_v(f)$ for the labeled areas. Boxes 1–3 are dominated by ABS from bubbles. Box 4 is associated with microstructure along the salt wedge interface. The red lines show the forward modeled S_v spectra based on the bubble distributions in (c). (c) Inferred bubble size distributions from fits to the spectra in (b). Results from box 1 for frequencies less than 160 kHz may be biased low due to excess attenuation near the front’s surface expression. Thus, the densities in (c) may be biased low for the larger bubble sizes.

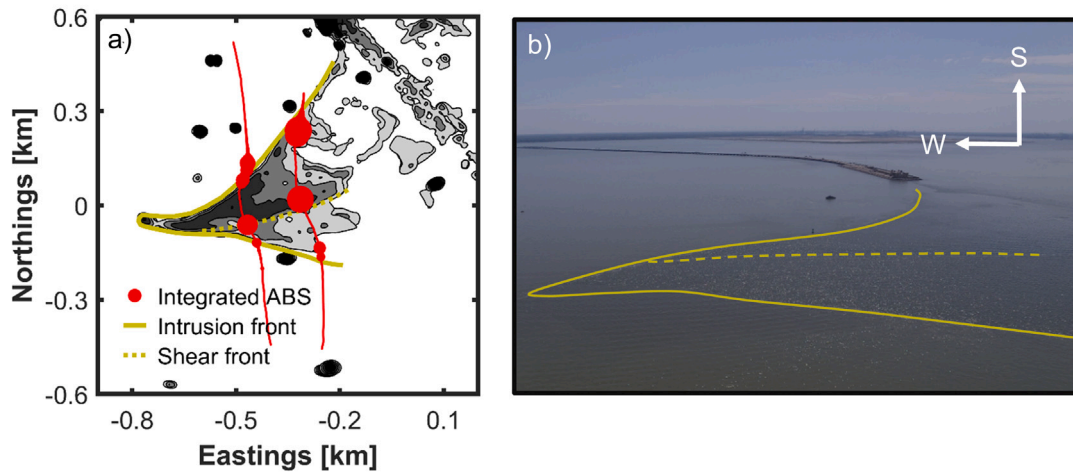


Fig. 9. (a) X-band radar data showing areas of elevated surface roughness from fronts, vessels, and buoys. The radar image represents an 80 s average around 11:42 on 24 April and the vessel transects correspond to the period from 11:33–11:55. The frontal boundaries were manually traced based on the roughness contours of the radar image. Increases in integrated, near-surface ABS of up to 5 orders of magnitude are associated with bubbles at frontal crossings. (b) A sUAS image from 11:56 with manually drawn boundaries based on foam in the images showing the fronts in (a). The cardinal direction annotations are approximate. Images of the front in (b) without annotations are included in the supplemental material.

signals were measured, but more ABS from ambient stratification was observed.

Through their synoptic imaging capabilities, echosounders provide evidence of stratification and instabilities with high spatial resolution. Here, we focus first on qualitative comparisons of the ABS imagery with results from in situ profiles. We then present quantitative assessments of the strength of turbulence using in situ profiles and acoustic inversions to demonstrate reasonable agreement between the techniques.

Using physical oceanographic measurements, the Richardson number is used to indicate regions where active mixing is expected. Areas

where velocity and CTD measurements yielded $Ri < 0.25$, indicating instability, are overlaid on echograms in Fig. 10. There is general agreement between these approaches with the echograms providing visual evidence of shear instabilities. On 21 April these instabilities were only associated with the salt wedge and a hydraulic transition near the tunnel. Increased stratification on 25 April led to multiple layers where $Ri < 0.25$ that were also identified acoustically. Where $Ri > 0.25$, suggesting stable stratification, at least at the scales resolved with the sampling methods, echograms reveal thin interfaces indicating a lack of active mixing/overturning. There were also areas of the

transects where echograms reveal shear instabilities, but Ri calculations did not suggest instability. In some cases this may be explained by the temporal evolution of instabilities that were initiated with $Ri < 0.25$ but had subsequently increased due to the development of the instability. Also, the scales at which $Ri < 0.25$ were not always resolved by the ADCP, which required vertical scales of at least 1 m to adequately resolve the vertical shear. The acoustic imaging of the shear instabilities has significantly higher vertical resolution, thereby providing more robust documentation of the occurrence of shear-induced mixing than could be obtained by Ri estimation.

Estimates of ϵ , χ_S , and other parameters were made using the microstructure profiler (Fig. 11). For a transect on 21 April, the highest values of ϵ and χ_S were located in the frontal region with values exceeding 10^{-4} W/kg and 10^{-3} PSU²/s, respectively. The elevated mixing at the pycnocline coincided well with ABS data showing relatively large amplitude (>1 m) shear instabilities. Values of ϵ and χ_S , were

also estimated using the echosounders (Fig. 12) and were in general agreement with the results from the microstructure profiler.

Properly identifying the scale of the unstable stratified shear layer is important since ϵ is dependent on the square of unstable shear layer thickness for a given bulk shear, stratification, and Richardson number (Kunze et al., 1990; Polzin, 1996; Jurisa et al., 2016). On 21 April, the regions of marginally unstable Ri corresponded to the shear instabilities observed acoustically in the pycnocline (Fig. 10). However, sampling resolution and noise in the density and velocity data can lead to uncertainties in estimates of the unstable shear layer thickness. When shear instabilities are visible in ABS data, their amplitude can provide a more accurate estimate of the unstable shear layer thickness. The thickness and location of this layer in the pycnocline on 21 April was determined by visually identifying the shear instabilities from the echogram, which qualitatively agreed with methods based on velocity magnitude and shear criteria. This layer clearly encompasses the low Ri region containing elevated dissipation values (Figs. 10–12).

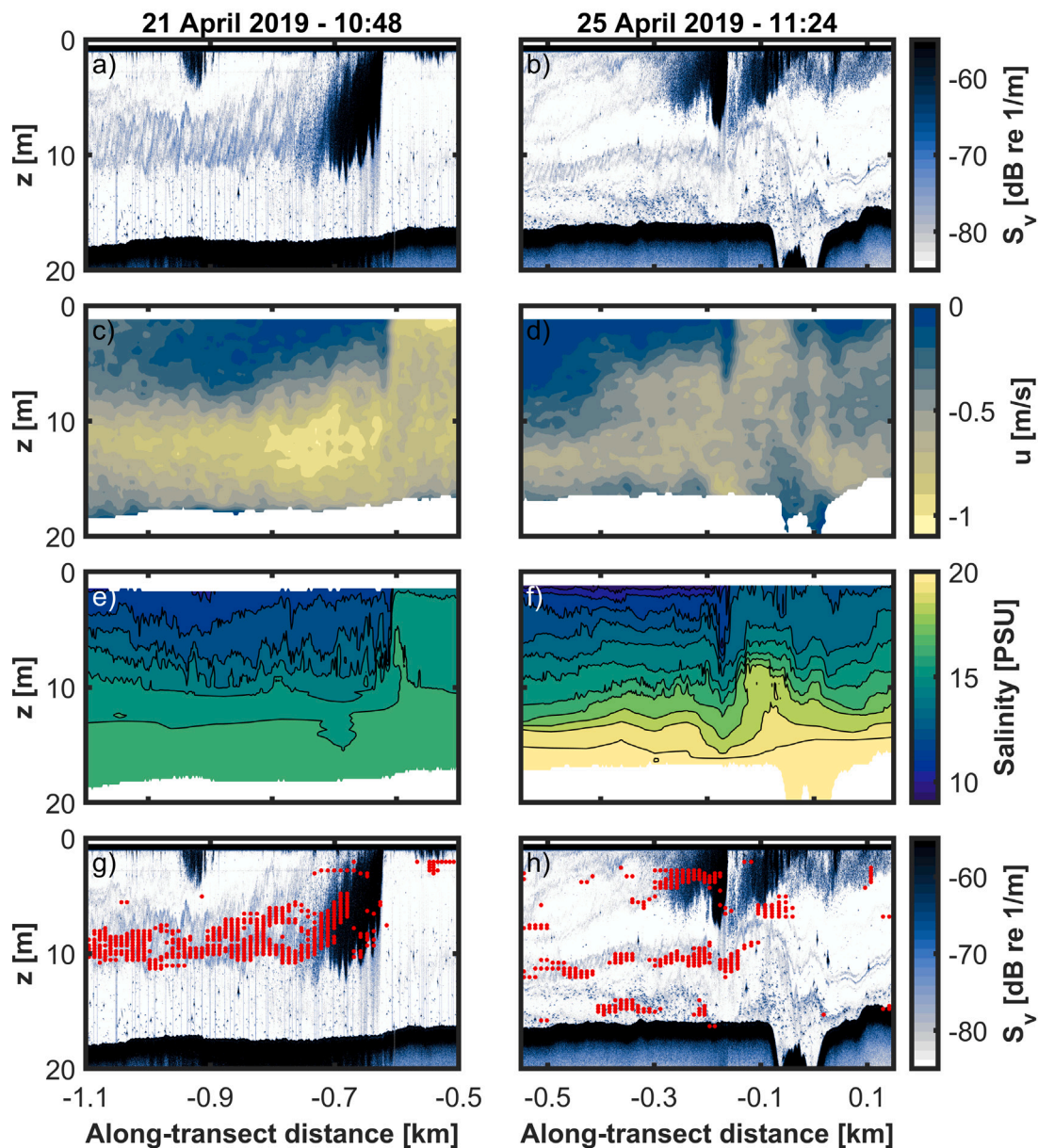


Fig. 10. (a,b) Echograms (70 kHz) showing volume backscattering for transects on 21 April (left) and 25 April (right). Panels (c,d) and (e,f) show measurements of velocity and salinity, respectively. (g,h) The same echograms as shown in (a,b) highlighting areas where $Ri < 0.25$ and $N > 0.05$, indicating hydrodynamic instabilities and active mixing. The $N > 0.05$ threshold limits the identification of areas where $Ri < 0.25$ but there is limited buoyancy flux due to weak density gradients.

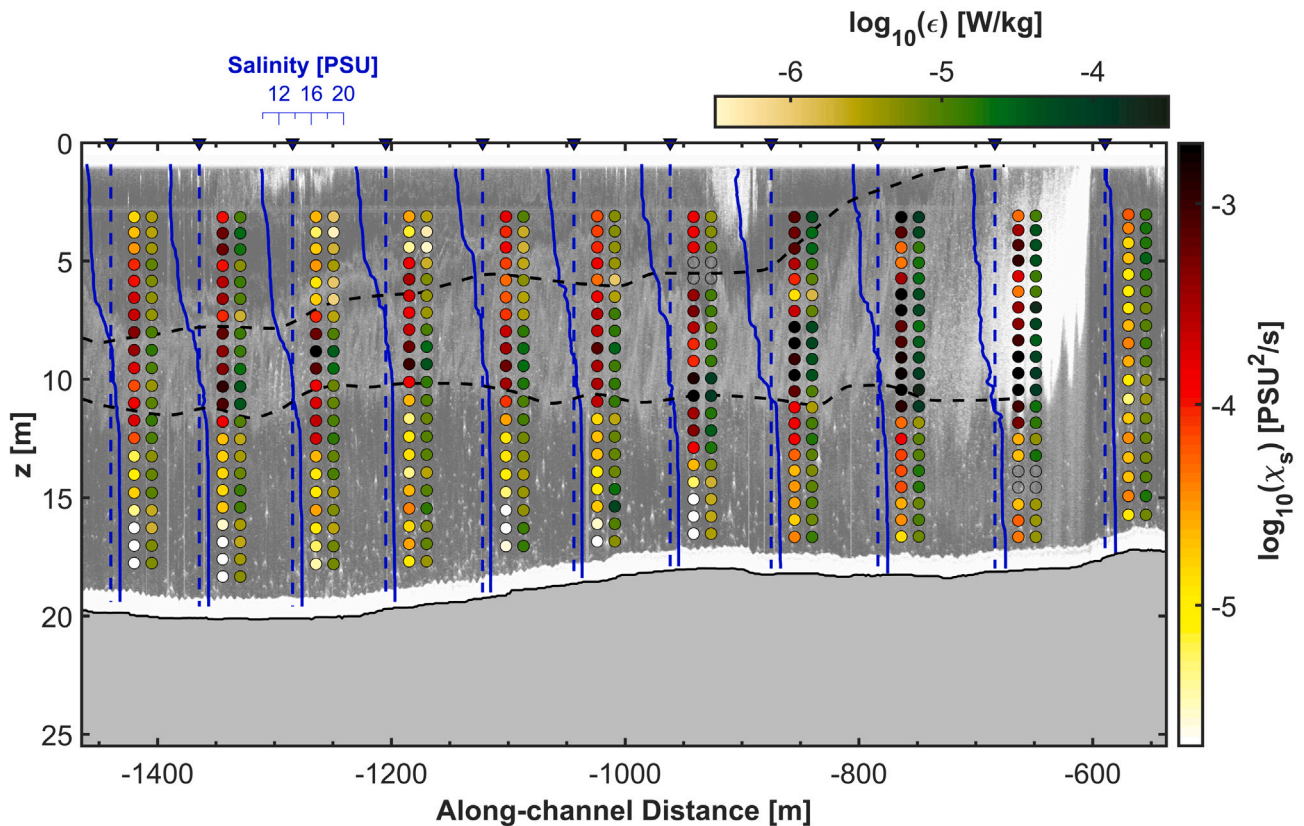


Fig. 11. An echogram overlaid with measurements derived from the profiler on 21 April. Profile locations are indicated by the blue triangles and dashed lines. The dots, placed just right of the profile location, indicate estimated values of the χ_s and ϵ , respectively. The area corresponding to the manually determined location and thickness of the unstable shear layer, which decreases with distance from the front, is shown by the dashed black lines.

Acoustically inferred estimates of ϵ and χ_s are shown in Fig. 12 corresponding to the same period as the in situ measurement techniques (Fig. 11). The difference in resolution makes detailed comparisons difficult, but overall agreement between the two methods is good. Both approaches yield similar dynamic ranges with ϵ ranging from approximately 10^{-6} W/kg to greater than 10^{-4} W/kg and χ_s between approximately 10^{-5} to 10^{-3} PSU^2/s . Decreasing values of both parameters were observed farther from the front. These inversions are performed at horizontal scales that exceed the resolution of in situ estimates by close to two orders of magnitude and vertical scales that resolve individual instabilities. Combined, this demonstrates the independent capabilities of echosounders to generate high-resolution estimates of turbulence parameters, informed by in situ measurements, and to also provide meaningful information to better constrain assumptions in the processing of in situ data.

ABS from interfaces became increasingly common later in the experiment as tidal forcing decreased and water mass intrusions from near the mouth of the estuary and Chesapeake Bay propagated further upstream. These interfaces are well-defined and thin ($\ll 1$ m) in the echograms (Fig. 13). Although active mixing may be occurring at these interfaces, Richardson numbers indicate stability at the sampling resolution of the physical oceanographic measurement techniques. The strongest observed salinity and temperature gradients, 5 PSU/m and 2 $^\circ\text{C}/1$ m, respectively, correspond to the diffuse scattering at approximately 2 m above the seabed. However, numerous interfaces higher in the water column correspond to weaker gradients. Specifically, for depths shallower than 13 m the interfaces correspond to changes of less than 0.05 $^\circ\text{C}$ and 0.15 PSU in adjacent 10 cm bins. These results are consistent with prior observations (e.g., Duda et al. (2016) and Stranne

et al. (2017)) that demonstrate that broadband echosounders can measure echoes associated with relatively small changes in temperature and density.

The observations in Fig. 13 show numerous biological targets, likely small fish, in the vicinity of these interfaces. When present, these targets generally result in higher levels of observed scattering than the interfaces themselves and care is required to separate these signals. A weak frequency dependence of scattering from these interfaces was observed and suggests the gradients in water properties were the dominant source of scattering (as opposed to zooplankton, which would be expected to follow an f^4 dependence — see supplemental material). Nonetheless, such interfaces may play a role in aggregating biological scatterers including zooplankton (McManus et al., 2003, 2005), which may generally affect observed levels of backscatter.

4.3. Suspended sediment

Two dominant patterns emerge from the turbidity measurements. First, as the experiment progressed the maximum OBS levels decreased (Fig. 14). Early in the experiment, near-bottom turbidity exceeded 100 NTU and was consistent with local resuspension of sediment. By the end of the experiment, the turbidity was less than 25 NTU throughout the water column. Areas of ABS attributed to suspended sediment (i.e., those where $S_V(f) \sim f^4$) were selected from all days with along-channel sampling and processed for comparison to OBS measurements. An example echogram, turbidity measurements, and ABS spectra for one transect show good agreement between areas with elevated OBS and ABS consistent with suspended sediment (Fig. 15).

As discussed in Section 3.3, the seabed near the front was dominated by fine to medium sands while more distant samples and Perkey et al.

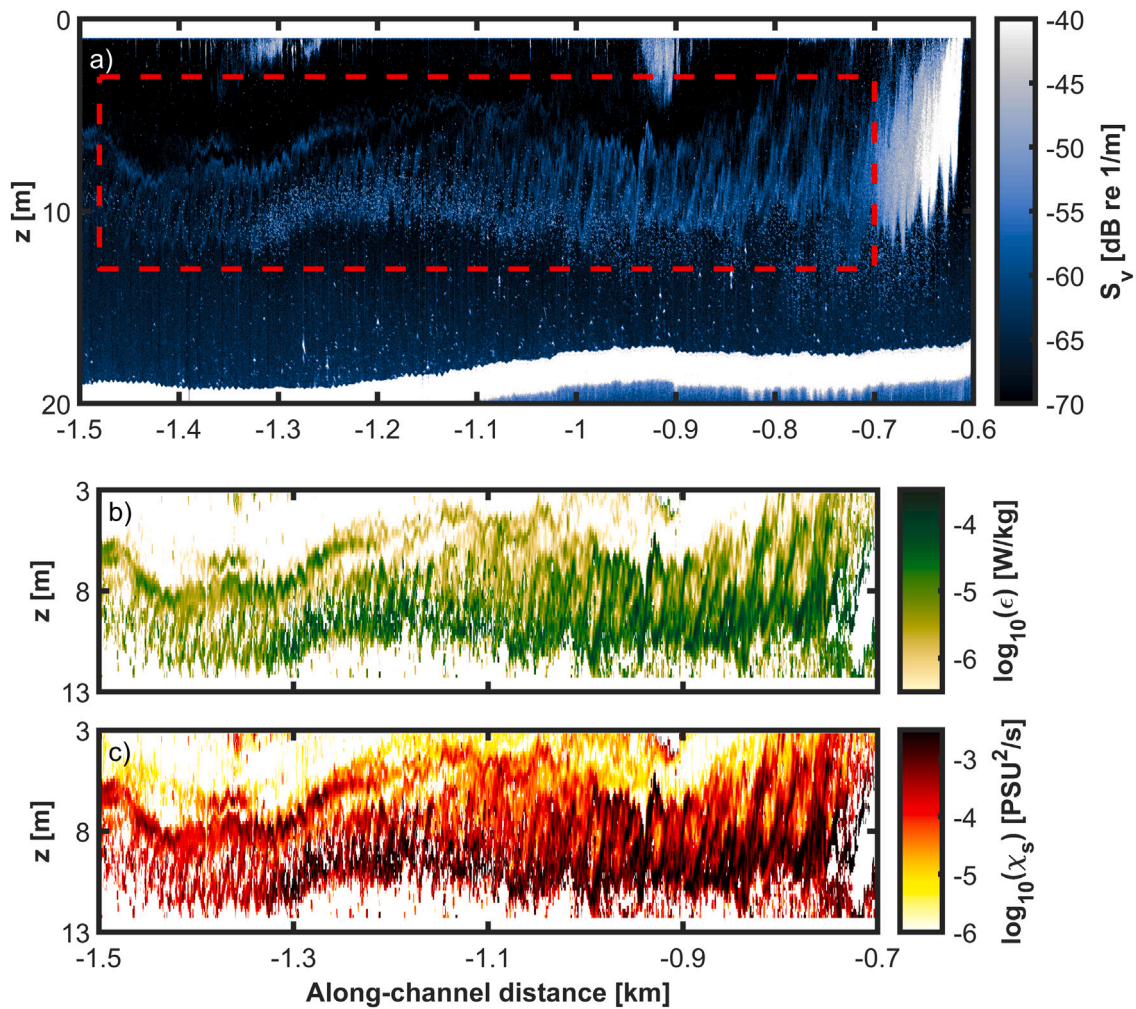


Fig. 12. (a) Echogram (70 kHz) showing volume backscattering from a single transect on 21 April. The dashed box shows the area emphasized in (b–c). The dominant feature in the selected area is a long train of shear instabilities formed between the tidal intrusion front (to the right) and the intruding salt wedge (propagating to the left in the lower layer). (b) Acoustically inferred dissipation rates of turbulent kinetic energy. (c) Acoustically inferred dissipation rates of salinity variance. Note areas in (b) and (c) that are white have either been removed from the data due to spectral fits implying scattering associated with other processes, or the inferred values fall below the dynamic range of the plot.

(2020) point to cohesive sediments. Eroded flocs from surface of the cores obtained from the two closest sites to the tidal intrusion from had size distributions with D_{50} [D_{10} , D_{90}] values of 270 μm [150 μm , 950 μm] and 380 μm [190 μm , 750 μm], respectively. Example models of $TS(f)$ are shown in Fig. 16a for a floc and sand grain that would lead to comparable inferred SSC values for a given level of ABS given the properties from Perkey et al. (2020). Although the modeled target strength spectrum for a comparably sized grain of sand is much higher than for a floc, its density is also higher. These terms counteract each other in Eqs. (12)–(17) such that similar SSCs could be obtained for either set of properties.

Given that Rouse numbers during portions of the flood tide were estimated to be less than 2.5, ABS from suspended sediment cannot be neglected. Comparisons between ABS, acoustically-inferred SSC values, and OBS measurements are shown in Fig. 16b–c. The slope of linear regressions between inferred SSC and versus measured NTU values fell between 0.5–2 for floc diameters from 181–420 μm , but comparable relationships could be obtained using the properties of sands in the area. Comparisons between Rouse profiles calculated using sand and flocs suggest that the relatively high SSCs many meters above the seabed are likely attributed to flocs. Suspended sediment concentration profiles predicted from Rouse using the parameters in Section 3.3 suggest that for sands the SSC 5 m above the seabed would be approximately 1% of that observed at 1 m. For flocs, Rouse profiles predict SSC at 5 m that is

about 1/3 of the concentration at 1 m above the seabed, which is more like the vertical distribution of turbidity in Fig. 14. Resuspended flocs are therefore more likely to explain the observed profiles of turbidity and near-bed ABS.

Inferred SSC values based on log-normal distributions with different means and standard deviations were also considered. For flocs, similar results are obtained although D_{50} sizes were smaller (~ 150 – 250 μm) than for calculations including a single size class due to the presence of the larger particles. The use of log-normal distributions did not significantly affect the mean of the distributions that achieved good agreement between ABS and OBS measurements. While the acoustics do show that areas of elevated SSC could be measured, this analysis clearly demonstrates the fundamental limitations of the techniques and the critical role that physical sampling plays in constraining the scattering models.

More rigorous multi-frequency or broadband inversions (e.g., Fromant et al. (2017)) are possible, but were not attempted for multiple reasons. The first is the lack of physical measurements for comparison to inversion results. Additionally, with all observations limited to the Rayleigh scattering regime, the measurements lack spectral structure that can be used to constrain the inversions. While inferred SSCs using this approach scale well with turbidity measurements, improved inversion approaches would benefit from higher operating frequencies where a transition in scattering regime could be observed.

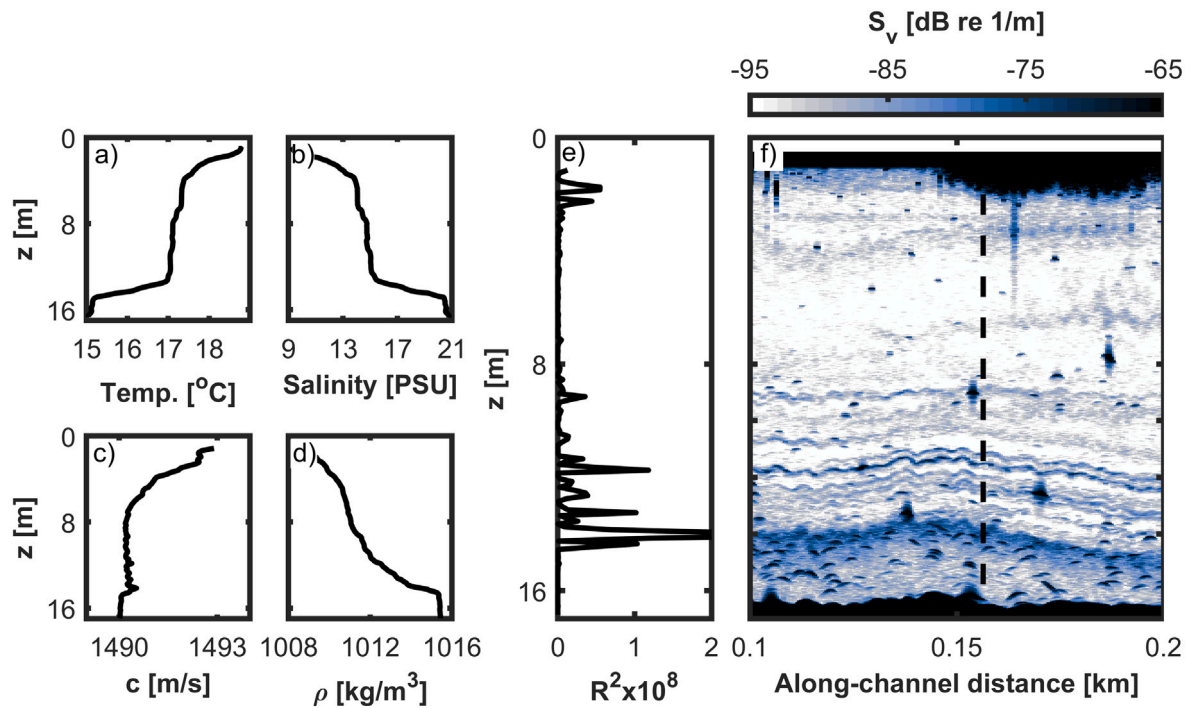


Fig. 13. (a–b) Temperature and salinity profiles. (c–d) Sound speed and density profiles. (e) Intensity reflection coefficient profile derived from (a–b). Note that the peak corresponding to the strong gradient near the seabed is cut-off to allow the smaller peaks associated with weaker gradients to be visible on this scale. (f) An echogram corresponding to the period from which the profiles are derived. The dashed line shows the time of the microstructure measurements although the acoustic sampling volume does not overlap with the location of the profile. Interfaces in the echogram correspond well to the peaks in (e).

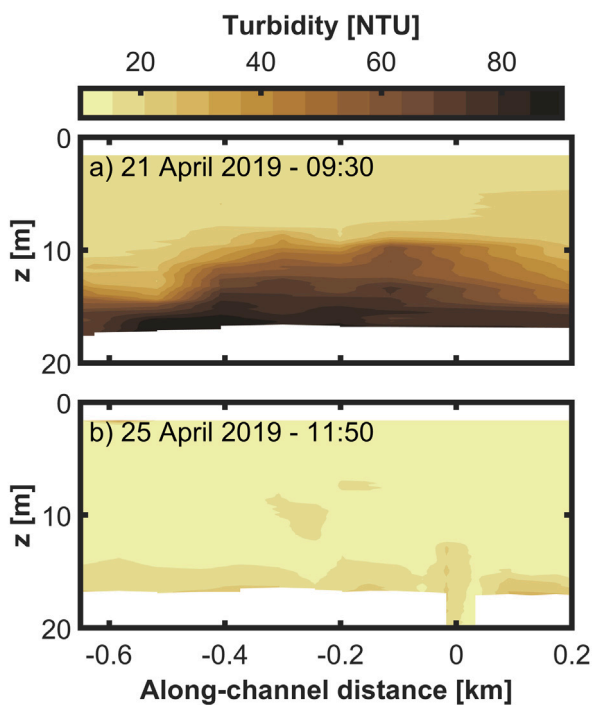


Fig. 14. Turbidity measurements from the profiler on 21 and 25 April at the same stage of the tide. Higher turbidity levels with strong increases near the seabed were observed early in the experiment (a). Lower levels of OBS were observed in ambient Chesapeake Bay and James River waters away from the seabed.

5. Discussion

At the James River tidal intrusion front, broadband acoustic backscattering measurements were used for synoptic imaging and to quantify and attribute acoustic backscattering to different sources including bubbles, mixing, stratification, suspended sediment, and biota. The results presented here are consistent with previously developed analytical models applicable to scattering in estuaries and demonstrate the value of acoustic remote sensing in environments with high spatial and temporal variability. When supported by in situ sampling techniques, high-frequency scattering measurements using echosounders can be used to obtain much higher resolution data that informs analyses relevant to physical, geological, and biological oceanographic studies.

A logical question to ask is: how applicable are these results to different estuarine environments, especially if different sampling frequencies are used to measure ABS? In other environments, the intensity and distribution of ABS will vary, but the dominant processes should remain the same. Thus, ABS should generally allow for the identification of dominant scattering sources when sufficient bandwidth is used (e.g., Figs. 2 and 7). The properties of each estuarine system will drive the spatial and temporal distribution of ABS, but published literature and our experience suggests the approach can be widely adopted.

Our observations in the James River and other field campaigns, including the Columbia River, Connecticut River, and Mobile Bay, provide examples to support this hypothesis. At these sites studies of ebb and flood fronts resulted in observations of the same dominant mechanisms with differences in their relative intensity and distribution. Furthermore, at individual sites the scattering and water column structure changes with the tidal cycle driving broader patterns (e.g., Figs. 10 and 14). Levels of ABS from turbulent microstructure are, for example, higher in the Connecticut River due to larger differences in the salinity between the ambient Long Island Sound waters and the river discharge while the role of suspended sediment is often less important (Lavery et al., 2013). There, bubbles contribute significantly to scattering in the ebb plume front, but over smaller spatial scales due to shallower

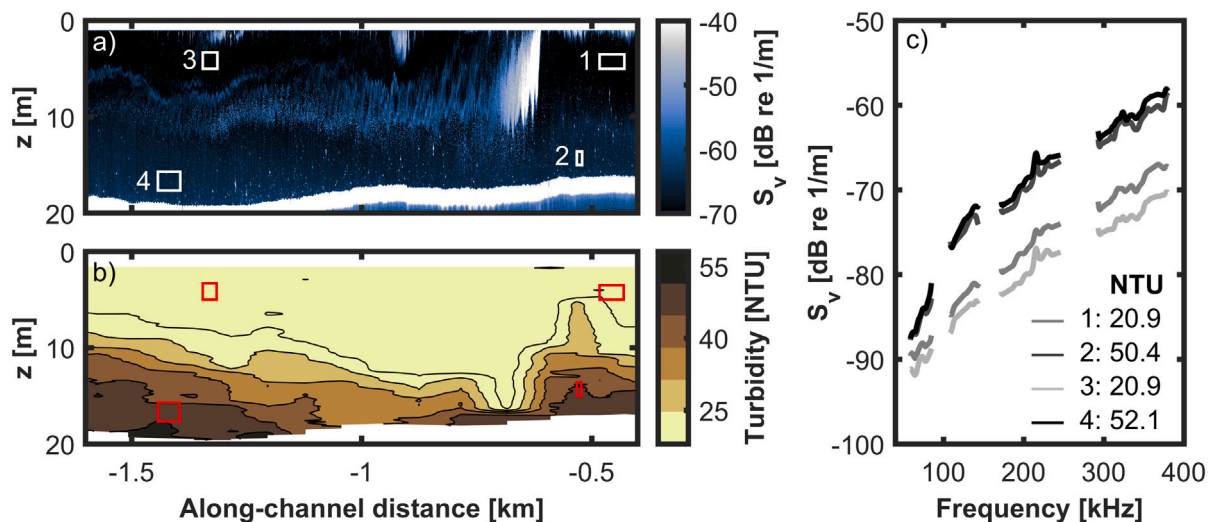


Fig. 15. (a) A 200 kHz echogram showing four areas selected for further processing. (b) Turbidity observations from the profiler. (c) S_v spectra for the areas shown in (a,b) labeled with the corresponding turbidity measurements. Note that the ABS and OBS sampled volumes may not overlap. Thus, ABS and OBS observations should scale similarly but 1:1 correspondence is not necessarily expected.

subduction (Bassett and Lavery, 2021). In contrast, unpublished data from Mobile Bay show much higher levels of ABS from biota and sediment resuspended during the flood tide than the James River observations. In Mobile Bay, complex ABS profiles from stratification were widely observed in addition to signals from bubbles and turbulent microstructure.

Referencing general characteristics of estuaries, the James River represents a partially mixed estuary (Geyer and MacCready, 2014). Acoustic measurements have been taken in environments spanning much of the estuarine parameter space from fjord-like systems (Muchowski et al., 2022) to time-dependent salt wedges like the Fraser, Columbia, and Connecticut Rivers (Geyer and Farmer, 1989; Kilcher and Moun, 2010; Lavery et al., 2013). Across these environments scattering from turbulent microstructure and stratification are common. While bubbles are cited less often, the presence of foam layers at frontal features is an indicator bubble generation with the potential for strong ABS. Marmorino and Trump (1996) and Kilcher and Moun (2010) include examples consistent with bubble entrainment.

Convergence at fronts and resulting bubble plumes were a common feature in the James River. Here, we observed no strong evidence that far from the front (>50 m) the intensity of the bubble plume was dependent on visual indicators of breaking (i.e., white caps). Even when breaking at the front was not identified visually, lines of foam on the surface and intense acoustic signals were still observed. This suggests widespread bubble entrainment even under calm conditions. Since small bubbles have strong acoustic signatures across the sampled bandwidth they dominate ABS even when vigorous mixing is occurring and signals from turbulent microstructure would otherwise be observed. Due to the spectral slopes associated with other processes the relative importance of bubbles is highest when fronts are sampled using instruments operating below ~100 kHz.

The use of lower-frequency transducers would have added benefits for inferring bubble distributions. Limited evidence of roll-off at the lowest frequencies attributed to bubbles was observed in this study. At depths of 10 m or less, bubbles with radii of $\approx 100 \mu\text{m}$ would be resonant at the lowest frequencies used in this study (50 kHz). Given the measured downwelling velocities, bubbles of this size are expected to be common within the observed plumes in the James River and other estuarine environments. Identifying the spectral roll-off associated with the resonance of the largest bubbles would require moving to lower frequencies. This poses challenges since lower-frequency transducers are generally larger and more difficult to deploy on small platforms. In

contrast, inversions for suspended sediment concentrations or the abundance of zooplankton would benefit from the use of higher-frequency transducers than those used here (i.e., $f \geq 500 \text{ kHz}$). Ideally, operational frequencies would resolve the transition between scattering regimes providing an indication of the size of scatterers. However, since most commercial off-the-shelf systems do not operate across the full range frequencies that would ideally be used to measure all of the processes in estuarine environments, there are inherent trade-offs in selecting instrumentation.

More common in estuarine applications are instruments that operate closer to or beyond the upper end of data presented here. ADCPs commonly operate in the 100 s of kHz or even 1 MHz range, while echosounders that can be easily deployment in for estuarine studies are common in the 100–350 kHz range. In estuarine environments, scattering from turbulent microstructure and suspended sediment generally, but not uniformly, increases with frequency over these ranges. In other coastal environments, particularly those where salinity gradients are much weaker, frequency-dependent scattering associated with turbulent microstructure would not follow the same patterns (Lavery et al., 2003, 2010a). Regardless, without significant bandwidth, discriminating between scattering sources in the absence of physical sampling can be difficult. For example, at 60 kHz more than 55 dB in dynamic range was observed in spectra (Figs. 2 and 7). This range was approximately 35 dB at 400 kHz with most observations being distinguished by much smaller margins. At these high frequencies the common scattering sources can result in similar ABS intensities under reasonable constraints. Therefore, the use of multiple channels with close to an order of magnitude of bandwidth is recommended to maximize source attribution capabilities.

Even with considerable bandwidth, acoustic sampling has inherent limitations. Multiple sources of scattering often occupy the same volume and measured ABS therefore represents their joint contributions. In this study overlap between turbulent microstructure and bubbles near the front and suspended sediment with biological scatterers provide two such examples. This can result in mixed acoustic spectra (e.g., Lavery et al. (2010a) and Bassett et al. (2018)) representing both processes or in masking of the echoes from the process that results in weaker scattering. This latter situation is well-represented in Fig. 7 where bubbles mask turbulent microstructure near the front. Any spectrum where processes overlap can impact forward and inverse methods and care must be taken not to conflate signals derived from different sources. Physical sampling, which is needed to provide inputs to scattering

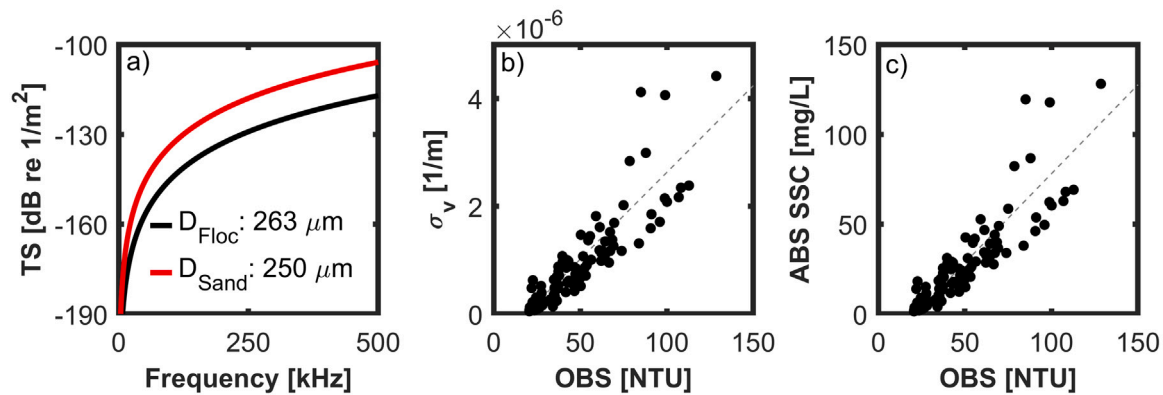


Fig. 16. (a) TS versus frequency for two sizes of suspended sediments. Modeled as fluid spheres, the acoustics properties for the floc and sand are $g = 1.29$, $h = 0.97$ and $g = 2.62$, $h = 3.89$, respectively. Both sets of sizes and properties can produce in good agreement between acoustically inferred SSC and OBS. (b) ABS versus OBS measurements. (c) A comparison between acoustically inferred SSC versus turbidity using the floc properties in (a). These were chosen to produce a fit with a slope of 1, but floc diameters from 181–420 μm result in slopes from 0.5–2.

models, can also be used to reduce potential biases associated with overlapping scattering processes.

Another factor in the interpretation of volume scattering spectra is that they are inherently noisy. Reducing this noise requires averaging, which requires assumptions about the spatial homogeneity of the process. The uncertainties inherent in the application of spectral processing have received little attention and should be the focus of future studies. Given that this requires robust comparisons to in situ sampling techniques, such work will be challenging. Nonetheless, better understanding these uncertainties through physical sampling and models would help to constrain the capabilities of ABS measurements.

Beyond discriminating among sources of ABS, even with existing uncertainties, multi-channel, broadband systems provide unparalleled sampling resolutions. This high-resolution acoustic imaging is an effective tool for resolving the dynamics of turbulent, stratified flows, particularly as it complements in situ measurements. The acoustic imaging of shear instabilities provides unambiguous evidence of the distribution of stratified turbulence. In the absence of confounding acoustic scatterers, the spectral analysis of the broadband signals provides quantitative estimates of the intensity of turbulence. Frontal structures are better resolved with acoustics than any in situ methods, due to the nearly continuous imaging capability echosounders. This study shows that the backscattering sources differ throughout frontal regions due to the varying contributions of bubbles, turbulence, interfaces, and suspended sediment, so the interpretation of the imagery is significantly augmented by supporting in situ measurements.

In this study ping rates were 5–10 Hz and the acoustic footprints were less than 2 m in diameter throughout most of the water column. In contrast to narrowband systems, broadband systems of the same frequency can achieve higher range resolution (Chu and Stanton, 1998) (e.g., less than a few cm for those discussed herein). As a result, in relatively shallow water (<100 m) nearly the entire water column along transects can be sampled. In contrast, the towed CTD array sampled continuously at along-transect but with limited vertical resolution (~2 m) while the distance between profiles was ~100 m. In deeper waters where slower ping rates are required and attenuation limits sampling range, full resolution of the water column cannot always be achieved. Additional vertical ambiguity is also introduced by the spherically spreading beam. Nonetheless, even dense arrays or profiling instruments for physical sampling cannot achieve the spatial resolution needed to adequately resolve many features observed in rapidly evolving environments.

Herein, no attempts were made to predict or invert acoustic scattering associated with interfaces, despite numerous published models for scattering from stratification (Fisher and Squier, 1975; Penrose and Beer, 1981; Lavery and Ross, 2007; Ross and Lavery, 2011; Stranne

et al., 2017, 2018; Weidner et al., 2020; Weidner and Weber, 2021).

This choice reflects the assumptions inherent in those models and questions about their applicability. For example, common assumptions include that the scattering is associated with plane waves at normal incidence with an acoustically smooth interface. Some, but not all, of these models assume the thickness of the interface is thin relative to the pulse length and many also assume a known range dependence. The validity of this general set of assumptions and their relative impacts on the acoustic inferences is unclear. Thus, while the ability to observe these interfaces is unambiguous, we refrain from attempting forward or inverse modeling of this scattering and instead recommend further development and evaluation of a more generalized scattering model for these interfaces. Such a model could be used to evaluate the simplifying assumptions regarding, plane waves, incidence angles, roughness, and range dependence, particularly at relatively short ranges where the ensonified volume may contain a limited number of Fresnel zones.

Different sources of noise can interfere with and complicate the processing and interpretation of echosounder measurements. Electrical noise is a notable challenge. In this study the echosounders were strongly affected by the use of the ADCP. This noise was electrical, not acoustic, and resulted in narrowband spikes that increased the noise floor of the echograms. While independent power supplies and batteries reduced this noise, it could not be fully isolated. The noise was present anytime the ADCP's independent power supply was used, even if the ADCP was not actively pinging. Noise impacts can often be reduced in post-processing, but this does not mitigate the impacts of reduced signal-to-noise ratios on real-time observations, which can mask low-intensity echoes.

Other challenges to interpretation of data are related to scattering driven by anthropogenic sources, rough surface conditions for vessel-based transducers, and multiple scattering near fronts. Cavitation from propellers and bubble entrainment by vessel hulls result in plumes that appear similar to those entrained by fronts. While these plumes do not persist as long, they can mask ambient sources of backscattering. When conditions are rough and transducers are mounted near the surface widespread bubble entrainment may also degrade system performance.

Multiple scattering, which occurs when the density of scatterers is high and signals scattered from one particle are re-scattered from neighboring particles, may appear to distort the apparent shape and intensity of features of interest. Clear indicators of multiple scattering in echograms include echoes located below the actual position of scatterers (e.g., fish schools appearing below the seabed) and excess attenuation (Stanton, 1984). Examples consistent with multiple scattering were only observed within a few meters of the fronts. In these cases the bubble plume appears to have a “tail” extending below the areas of the plume (Figs. 5a and 7). In extreme cases, the apparent

plume depth occupied the full water column, although thresholding of the data to intensities consistent with adjacent portions of the plume was sufficient to extract the plume shape. Multiple scattering and excess attenuation of the seabed were observed primarily in channels with center frequencies less than 120 kHz (Bassett and Lavery, 2021). Increased excess attenuation at lower frequencies may be attributed, in part, to the higher ratio of the extinction to scattering cross sections for resonant bubbles at low frequencies (Stanton, 1983; Trevorrow, 2003).

Although ship-based sampling is generally more efficient, sampling with underwater vehicles or tow bodies has unique benefits. A REMUS 100 vehicle equipped with two broadband echosounders (Bassett et al., 2021) was deployed in the James River experiment. The vehicle had lower levels of electrical noise than the echosounders on *R/V Tidewater*. This improves the quality of the imaging and the spectra derived from the data. In addition, up-ward looking echosounders can better sample the near-surface region that falls within a vessel-deployed unit's near-field. The echosounder equipped REMUS 100 obtained quality data up to the point where the processing sidelobes from the surface dominate (Lavery et al., 2017), which was approximately 40 cm. This approach has proven valuable in other related field campaigns focusing on shallow plume fronts where missing the upper 1–2 m of the water column represents a loss of most of the signal of interest.

6. Conclusions

Broadband echosounding is a powerful remote sensing approach that can provide imaging and quantitative information about scattering mechanisms at spatial scales that cannot otherwise be achieved using physical sampling techniques. In estuarine environments, bubbles, mixing, interfaces, suspended sediment, and biological scatterers are all common. The right choice of operating frequencies allows for some quantification of all of these scattering sources. In this study broadband acoustic scattering measurements coupled with analytical models for sources of scattering including stratified turbulence and suspended sediment yield favorable comparisons to in situ measurements. Inversions to estimate bubble size distributions cannot be validated, but are consistent with power-law dependencies reported previously in the literature. Scattering from sharp interfaces and biology are also well-resolved.

While the use of echosounders can be beneficial simply due to their imaging capabilities, supporting physical measurements including ADCPs, CTDs, optical backscattering sensors, and sediment samples can help constrain key inputs to analytical scattering models used to invert echosounder data for oceanographic parameters. Appropriate scattering models already exist for the dominant scattering processes generally encountered in estuarine environments. Given the potential benefits, quantitative use of acoustic scattering methods should be more widely adopted, particularly in rapidly evolving coastal environments where traditional measurement techniques result in valuable, but highly undersampled data.

Declaration of competing interest

The authors declare that they have no known competing financial interests or personal relationships that could have appeared to influence the work reported in this paper.

Data availability

Data will be made available on request.

Acknowledgments

The authors gratefully acknowledge the comments provided by three anonymous reviewers. Their reviews were thorough and undoubtedly improved the quality of this paper. Our work was sponsored by the U.S. Office of Naval Research (ONR) under the UnderSea Remote Sensing (USRS) Departmental Research Initiative. We thank Dr. Reginald Beach for supporting the different research activities under USRS. WHOI engineers Beb Pettit and Jay Sisson were instrumental in *R/V Tidewater* systems development and field operations. We also acknowledge the efforts of, and discussions with, other USRS collaborators including Autumn Kidwell, Craig McNeil, Andrey Shcherbina, Trina Litchendorf, Tim Martson, Dan Plotnick, Joe Calantoni, and Ben Reeder.

Appendix A. Supplementary data

Supplementary material related to this article can be found online at <https://doi.org/10.1016/j.pocan.2023.103167>.

References

- Al-Lashi, R.S., Gunn, S.R., Czerski, H., 2016. Automated processing of oceanic bubble images for measuring bubble size distributions underneath breaking waves. *J. Atmos. Ocean. Technol.* 33 (8), 1701–1714. <http://dx.doi.org/10.1175/JTECH-D-15-0222.1>.
- Anderson, V.C., 1950. Sound scattering from a fluid sphere. *J. Acoust. Soc. Am.* 22 (4), 426–431. <http://dx.doi.org/10.1121/1.1906621>.
- Baschek, B., Farmer, D.M., Garrett, C., 2006. Tidal fronts and their role in air-sea gas exchange. *J. Mar. Res.* 64, 483–515. <http://dx.doi.org/10.1357/002224006778715766>.
- Bassett, C., De Robertis, A., Wilson, C.D., 2018. Broadband echosounder measurements of the frequency response of fishes and euphausiids in the gulf of alaska. *ICES J. Mar. Sci.* 75 (3), 1131–1142. <http://dx.doi.org/10.1093/icesjms/fsx204>.
- Bassett, C., Lavery, A.C., 2021. Observations of high-frequency acoustic attenuation due to bubble entrainment at estuarine fronts. *Proc. Mtg. Acoust.* 45, 005001. <http://dx.doi.org/10.1121/2.0001539>.
- Bassett, C., Lavery, A.C., Pettitt, R., Loranger, S., 2021. Autonomous platforms for measuring broadband backscatter. *Proc. Mtg. Acoust.* 45, 1–10. <http://dx.doi.org/10.1121/2.0001654>.
- Breitz, N., Medwin, H., 1989. Instrumentation for in situ acoustical measurements of bubble spectra under breaking waves. *J. Acoust. Soc. Am.* 86 (2), 739–743. <http://dx.doi.org/10.1121/1.398196>.
- Caruthers, J.W., Elmore, P.A., Novarini, J.C., Goodman, R.R., 1999. An iterative approach for approximating bubble distributions from attenuation measurements. *J. Acoust. Soc. Am.* 106 (1), 185–189. <http://dx.doi.org/10.1121/1.427047>.
- Chen, C., Millero, F., 1977. Speed of sound in seawater at high pressures. *J. Acoust. Soc. Am.* 62 (5), 1129–1135. <http://dx.doi.org/10.1121/1.381646>.
- Chu, D., Stanton, T.K., 1998. Application of pulse compression techniques to broadband acoustic scattering by live individual zooplankton. *J. Acoust. Soc. Am.* 104, 39–55.
- Cummins, P.F., Armi, L., Vagle, S., 2006. Upstream internal hydraulic jumps. *J. Phys. Oceanogr.* 36 (5), 753–769. <http://dx.doi.org/10.1175/JPO2894.1>.
- Dahl, P.H., Jessup, A.T., 1995. On bubble clouds produced by breaking waves: An event analysis of ocean acoustic measurements. *J. Geophys. Res.* 100 (C3), 5007–5020. <http://dx.doi.org/10.1029/94JC03019>.
- Deane, G.B., Stokes, M.D., 2002. Scale dependence of bubble creation mechanisms in breaking waves. *Nature* 418, 839–844. <http://dx.doi.org/10.1038/nature00967>.
- Demer, D.A., Andersen, L.N., Bassett, C., Berger, L., Chu, D., Condiotty, J., et al., 2017. 2016 USA–Norway EK80 Workshop Report: Evaluation of a wideband echosounder for fisheries and marine ecosystem science. *ICES Coop. Res. Rep. No. 336*, <http://dx.doi.org/10.17895/ices.pub.2318>.
- Demer, D.A., Berger, L., Bernasconi, M., Bethke, E., Boswell, K., Chu, D., Domokos, R., et al., 2015. Calibration of acoustic instruments. *ICES CRR No. 326*, <http://dx.doi.org/10.25607/OBP-185>.
- Devin, C., 1959. Survey of thermal, radiation, and viscous damping of pulsating air bubbles in water. *J. Acoust. Soc. Am.* 31 (12), 1654–1667. <http://dx.doi.org/10.1121/1.1907675>.
- Dietrich, W.E., 1982. Settling velocity of natural particles. *J. Water Resour. Res.* 18 (6), 1615–1626. <http://dx.doi.org/10.1029/WR018i006p01615>.
- Downing, J., 2006. Twenty-five years with OBS sensors: The good, the bad, and the ugly. *Cont. Shelf Res.* 26 (17), 2299–2318. <http://dx.doi.org/10.1016/j.csr.2006.07.018>.
- Duda, T., Lavery, A., Sellers, C., 2016. Evaluation of an acoustic remote sensing method for frontal-zone studies using double-diffusive instability microstructure data and density interface data from intrusions. *Methods Oceanogr.* 17, 264–281. <http://dx.doi.org/10.1016/j.mio.2016.09.004>.

- Fall, K., 2020. Influence of Suspended Particle Size And Composition On Particle Image Processing, Estuarine Floc Fractal Properties, and Resulting Estuarine Light Attenuation (Ph.D. thesis). Virginia Institute of Marine Science.
- Farmer, D.M., Armi, L., 1999. Stratified flow over topography: the role of small-scale entrainment and mixing in flow establishment. *Proc. R. Soc. Lond. A* 455, 3221–3258. <http://dx.doi.org/10.1098/rspa.1999.0448>.
- Farmer, D.M., Dungan Smith, J., 1980. Tidal interaction of stratified flow with a sill in knight inlet. *Deep Sea Res. I* 27 (3), 239–254. [http://dx.doi.org/10.1016/0198-0149\(80\)90015-1](http://dx.doi.org/10.1016/0198-0149(80)90015-1).
- Fisher, F.H., Squier, E.D., 1975. Observation of acoustic layering and internal waves with a narrow-beam 87.5-kHz echo sounder. *J. Acoust. Soc. Am.* 58, 1315–1317. <http://dx.doi.org/10.1121/1.380815>.
- Fromant, G., Floch, F., Lebourges-Dhaussy, A., Joundin, F., Perrot, Y., Le Dantec, N., Delacourt, C., 2017. In situ quantification of the suspended load of estuarine aggregates from multifrequency acoustic inversions. *J. Atmos. Ocean. Technol.* 34, 1625–1643. <http://dx.doi.org/10.1175/JTECH-D-16-0079.1>.
- Gargett, A.E., Moum, J.N., 1995. Mixing efficiencies in turbulent tidal fronts: Results from direct and indirect measurements of density flux. *J. Phys. Ocean.* 25 (11), 2583–2608. [http://dx.doi.org/10.1175/1520-0485\(1995\)025<2583:MEITTF>2.0.CO;2](http://dx.doi.org/10.1175/1520-0485(1995)025<2583:MEITTF>2.0.CO;2).
- Geyer, W.R., Farmer, D.M., 1989. Tide-induced variation of the dynamics of a salt Wedge Estuary. *J. Phys. Ocean.* 19 (8), 1060–1072. [http://dx.doi.org/10.1175/1520-0485\(1989\)019<1060:TIVOTD>2.0.CO;2](http://dx.doi.org/10.1175/1520-0485(1989)019<1060:TIVOTD>2.0.CO;2).
- Geyer, W.R., Lavery, A.C., Scully, M.E., Trowbridge, J.H., 2010. Mixing by shear instability at high Reynolds number. *Geophys. Res. Lett.* 37 (22), L22607. <http://dx.doi.org/10.1029/2010GL045272>.
- Geyer, W.R., MacCready, P., 2014. The estuarine circulation. *Annu. Rev. Fluid Mech.* 46 (1), 175–197. <http://dx.doi.org/10.1146/annurev-fluid-010313-141302>.
- Goodman, L., 1990. Acoustic scattering from ocean microstructure. *J. Geophys. Res.* 95 (C7), 11557–11573. <http://dx.doi.org/10.1029/JC095iC07p11557>.
- Gregg, M., D'Asaro, E., Riley, J., Kunze, E., 2018. Mixing efficiency in the ocean. *Annu. Rev. Mar. Sci.* 10 (1), 443–473. <http://dx.doi.org/10.1146/annurev-marine-121916-063643>.
- Guillén, J., Palanques, A., Puig, P., De Madron, X., F. Nyffeler, F., 2000. Field calibration of optical sensors for measuring suspended sediment concentration in the western Mediterranean. *Sci. Mar.* 64 (4), 427–435. <http://dx.doi.org/10.3989/scimar.2000.64n4427>.
- Haidvogel, D.B., Arango, H., Budgell, W.P., Cornuelle, B.D., Curchitser, E., Di Lorenzo, E., Fennel, K., Geyer, W.R., Hermann, A.J., Lanerolle, L., Levin, J., McWilliams, J.C., Miller, A.J., Moore, A.M., Powell, T.M., Schepetkin, A.F., Sherwood, C.R., Signell, R.P., Warner, J.C., Wilkin, J., 2008. Ocean forecasting in terrain-following coordinates: Formulation and skill assessment of the Regional Ocean Modeling System. *J. Comput. Phys.* 227, 3595–3624. <http://dx.doi.org/10.1016/j.jcp.2007.06.016>.
- Haller, M.C., Honegger, D.A., Pittman, R., O'Dea, A., Simpson, A., 2019. Real-time marine radar observations of nearshore waves and flow structures from shore-based towers. In: 2019 IEEE/OES Twelfth Current, Waves and Turbulence Measurement (CWTM). pp. 1–7. <http://dx.doi.org/10.1109/CWTM43797.2019.8955152>.
- Hanes, D.M., Vincent, C.E., Huntley, D.A., Clarke, T.L., 1988. Acoustic measurements of suspended sand concentration in the C2S2 experiment at Stanhope Lane, Prince Edward Island. *Mar. Geol.* 81 (1), 185–196. [http://dx.doi.org/10.1016/0025-3227\(88\)90025-4](http://dx.doi.org/10.1016/0025-3227(88)90025-4).
- Haury, L., Briscoe, M., Orr, M., 1979. Tidally generated internal wave packets in Massachusetts bay. *Nature* 178, 312–317. <http://dx.doi.org/10.1038/278312a0>.
- Hay, A.E., 1983. On the remote acoustic detection of suspended sediment at long wavelengths. *J. Geophys. Res.* 88 (C12), 7525–7542. <http://dx.doi.org/10.1029/JC088iC12p07525>.
- Holleman, R.C., Geyer, W.R., Ralston, D.K., 2016. Stratified turbulence and mixing efficiency in a salt wedge estuary. *J. Phys. Ocean.* 46 (6), 1769–1783.
- Honegger, D.A., Haller, M.C., Geyer, W.R., Farquharson, G., 2017. Oblique internal hydraulic jumps at a stratified estuary mouth. *J. Phys. Ocean.* 47 (1), 85–100.
- Horner-Devine, A.R., Chickadel, C.C., 2017. Lobe-cleft instability in the buoyant gravity current generated by estuarine outflow. *Geophys. Res. Lett.* 44, 5001–5007. <http://dx.doi.org/10.1146/annurev-fluid-010313-141408>.
- Horner-Devine, A.R., Hetland, R.D., MacDonald, D.G., 2015. Mixing and transport in coastal river plumes. *Annu. Rev. Fluid Mech.* 47, 569–594. <http://dx.doi.org/10.1002/2017GL072997>.
- Jay, D.A., Pan, J., Orton, P.M., Horner-Devine, A.R., 2009. Asymmetry of Columbia River plume tidal fronts. *J. Mar. Syst.* 78, 442–459. <http://dx.doi.org/10.1016/j.jmarsys.2008.11.015>.
- Johnson, R.K., 1977. Sound scattering from a fluid sphere revisited. *J. Acoust. Soc. Am.* 61 (2), 375–377. <http://dx.doi.org/10.1121/1.381326>.
- Johnson, B., Cooke, R., 1979. Bubble populations and spectra in coastal waters: A photographic approach. *J. Geophys. Res.* 84 (C7), 3761–3766.
- Jurisa, J.T., Nash, J.D., Moum, J.N., Kilcher, L.F., 2016. Controls on turbulent mixing in a strongly stratified and sheared tidal river plume. *J. Phys. Ocean.* 46, 2373–2388. <http://dx.doi.org/10.1175/JPO-D-15-0156.1>.
- Kantha, L.H., Clayson, C.A., 1994. An improved mixed layer model for geophysical applications. *J. Geophys. Res.* 99 (C12), 25,235–25,266. <http://dx.doi.org/10.1029/94JC02257>.
- Kilcher, L.F., Moum, J.N., 2010. Structure and dynamics of the Columbia River tidal plume front. *J. Geophys. Res.* 115 (C05S90), 1–20. <http://dx.doi.org/10.1029/2009JC006066>.
- Kunze, E., Williams, A.J., Briscoe, M.G., 1990. Observations of shear and vertical stability from a neutrally buoyant float. *J. Geophys. Res.* 95 (C10), 18127–18142. <http://dx.doi.org/10.1029/JC095iC10p18127>.
- Largier, J.L., 1992. Tidal intrusion fronts. *Estuaries* 15 (1), 26–39. <http://dx.doi.org/10.2307/1352707>.
- Lavery, A.C., Bassett, C., Lawson, G., Jech, J.M., 2017. Exploiting signal processing approaches from broadband echosounder. *ICES J. Mar. Sci.* 75 (8), 2262–2275. <http://dx.doi.org/10.1093/icesjms/lsx155>.
- Lavery, A.C., Chu, D., Moum, J.N., 2010a. Measurements of acoustic scattering from zooplankton and oceanic microstructure using a broadband echosounder. *ICES J. Mar. Sci.* 67, 379–394. <http://dx.doi.org/10.1093/icesjms/fsp242>.
- Lavery, A.C., Chu, D., Moum, J.N., 2010b. Observations of broadband acoustic backscattering from nonlinear internal waves: Assessing the contribution from microstructure. *IEEE J. Ocean. Eng.* 35 (4), 695–709. <http://dx.doi.org/10.1109/JOE.2010.2047814>.
- Lavery, A.C., Geyer, W.R., Scully, M., 2013. Broadband acoustic quantification of stratified turbulence. *J. Acoust. Soc. Am.* 134 (1), 40–54. <http://dx.doi.org/10.1121/1.4807780>.
- Lavery, A.C., Ross, T., 2007. Acoustic scattering from double-diffusive microstructure. *J. Acoust. Soc. Am.* 122 (3), 1449–1462.
- Lavery, A.C., Schmitt, R.W., Stanton, T.K., 2003. High-frequency acoustic scattering from turbulent oceanic microstructure: The importance of density fluctuations. *J. Acoust. Soc. Am.* 114 (5), 2685–2697. <http://dx.doi.org/10.1121/1.1614258>.
- Lewis, E.R., Schwartz, S.E., 2004. *Sea Salt Aerosol Production: Mechanisms, Methods, Measurements, and Models*. American Geophysical Union, Washington, DC, p. 254.
- MacDonald, I.T., Vincent, C.E., Thorne, P.D., Moate, B.D., 2013. Acoustic scattering from a suspension of flocculated sediments. *J. Geophys. Res.* 118, 2581–2594. <http://dx.doi.org/10.1002/jgrc.20197>.
- Marmorino, G.O., Trump, C.L., 1996. High-resolution measurements made across a tidal intrusion front. *J. Geophys. Res.* 101 (C12), 25661–25647. <http://dx.doi.org/10.1029/96JC02384>.
- Mazzini, P.L.F., Chant, R.J., 2016. Two-dimensional circulation and mixing in the far field of a surface-advected river plume. *J. Geophys. Res.* 121, 3757–3776. <http://dx.doi.org/10.1002/2015JC011059>.
- McManus, M.A., Alldredge, A.L., Barnard, A., Boss, E.S., Case, J.F., Cowles, T.J., Donaghay, P.L., Eisner, L.B., Gifford, D.J., Greenlaw, C.F., Herren, C.M., Holliday, D.V., Johnson, D.W., MacIntyre, S., McGehee, D.M., Osborn, T.R., Perry, M.J., Pieper, R.E., Rines, J.E.B., Smith, D.C., Sullivan, J.M., Talbot, M., Twardowski, M., Weidemann, A.D., Zaneveld, J.R.V., 2003. Characteristics, distribution and persistence of thin layers over a 48-hour period. *Mar. Ecol. Prog. Ser.* 261, 1–19. <http://dx.doi.org/10.3354/meps261001>.
- McManus, M.A., Cheriton, O.M., Drake, P.J., Holliday, D.V., Storlazzi, C.D., Donaghay, P.L., Greenlaw, C.F., 2005. Effects of physical processes on structure and transport of thin zooplankton layers in the coastal ocean. *Mar. Ecol. Prog. Ser.* 301, 199–215. <http://dx.doi.org/10.3354/meps301199>.
- Medwin, H., 1970. In situ acoustic measurements of bubble populations in coastal ocean waters. *J. Geophys. Res.* 75 (3), 599–611. <http://dx.doi.org/10.1029/JC075i003p00599>.
- Medwin, H., 1977a. Acoustical determinations of bubble-size spectra. *J. Acoust. Soc. Am.* 62 (4), 1041–1044. <http://dx.doi.org/10.1121/1.381617>.
- Medwin, H., 1977b. In situ acoustic measurements of microbubbles at sea. *J. Geophys. Res.* 82 (6), 971–976. <http://dx.doi.org/10.1029/JC082i006p00971>.
- Medwin, H., Clay, C., 1998. *Fundamentals of Acoustics Oceanography*. Academic Press, Boston, MA, pp. 138–141.
- Millero, F.J., Chen, C., Bradshaw, A., Schleicher, K., 1980. A new high pressure equation of state for seawater. *Deep Sea Res. A* 27 (3–4), 255–264. [http://dx.doi.org/10.1016/0198-0149\(80\)90016-3](http://dx.doi.org/10.1016/0198-0149(80)90016-3).
- Moum, J.N., 1996. Efficiency of mixing in the main thermocline. *J. Geophys. Res.* 101 (C5), 12057–12069. <http://dx.doi.org/10.1029/96JC00508>.
- Moum, J.N., Farmer, D.M., Smyth, W.D., Armi, L., Vagle, S., 2003. Structure and generation of turbulence at interfaces strained by internal solitaries waves propagating shoreward over the continental shelf. *J. Phys. Ocean.* 33 (10), 2093–2112. [http://dx.doi.org/10.1175/1520-0485\(2003\)033<2093:SAGOTA>2.0.CO;2](http://dx.doi.org/10.1175/1520-0485(2003)033<2093:SAGOTA>2.0.CO;2).
- Muchowski, J., Umlauf, L., Arneborg, L., Holtermann, P., Weidner, E., Humborg, C., Stranne, C., 2022. Potential and limitations of a commercial broadband echo sounder for remote observations of turbulent mixing. *J. Atmos. Ocean. Technol.* 39 (12), 1985–2003. <http://dx.doi.org/10.1175/JTECH-D-21-0169.1>.
- Nash, J.D., Moum, J.N., 2002. Microstructure estimates of turbulent salinity flux and the dissipation spectrum of salinity. *J. Phys. Ocean.* 32 (8), 2312–2333. [http://dx.doi.org/10.1175/1520-0485\(2002\)032<2312:MEOTSF>2.0.CO;2](http://dx.doi.org/10.1175/1520-0485(2002)032<2312:MEOTSF>2.0.CO;2).
- Oakey, N.S., 1982. Determination of the rate of dissipation of turbulent energy from simultaneous temperature and shear microstructure measurements. *J. Phys. Ocean.* 12, 256–271. [http://dx.doi.org/10.1175/1520-0485\(1982\)012<0256:DOTROD>2.0.CO;2](http://dx.doi.org/10.1175/1520-0485(1982)012<0256:DOTROD>2.0.CO;2).
- Orr, M.H., Haury, L.R., Wiebe, P.H., Briscoe, M.G., 2000. Backscatter of high-frequency (200 kHz) acoustic wavefields from ocean turbulence. *J. Acoust. Soc. Am.* 108 (4), 1595–1601. <http://dx.doi.org/10.1121/1.1286883>.

- Pan, J., Jay, D., 2009a. Effects of ambient velocity shear on nonlinear internal wave associated mixing at the Columbia River plume front. *J. Geophys. Res.* 114 (C00B07), 1–13. <http://dx.doi.org/10.1029/2008JC004988>.
- Pan, J., Jay, D.A., 2009b. Dynamic characteristics and horizontal transports of internal solitons generated at the Columbia River plume front. *Cont. Shelf Res.* 29, 252–262. <http://dx.doi.org/10.1016/j.csr.2008.01.002>.
- Penrose, J.D., Beer, T., 1981. Acoustic reflection from estuarine pycnoclines. *Estuar. Coast. Shelf Sci.* 12, 237–249. [http://dx.doi.org/10.1016/S0302-3524\(81\)80122-3](http://dx.doi.org/10.1016/S0302-3524(81)80122-3).
- Perkey, D.W., Smith, S.J., Fall, K.A., Massey, G.M., Friedrichs, C.T., Hicks, E.M., 2020. Impacts of muddy bed aggregates on sediment transport and management in the tidal James River, VA. *J. Waterway, Port, Coastal, Ocean Eng.* 146 (5), 04020028. [http://dx.doi.org/10.1061/\(ASCE\)WW.1943-5460.0000578](http://dx.doi.org/10.1061/(ASCE)WW.1943-5460.0000578).
- Polzin, K.L., 1996. Statistics of the Richardson number: Mixing models and finestructure. *J. Phys. Ocean.* 26, 1409–1425.
- Pritchard, D.W., 1952. Salinity distribution and circulation in the Chesapeake Bay estuarine system. *J. Mar. Res.* 11 (2), 106–123. <http://dx.doi.org/10.1029/94JC02257>.
- Rayleigh, J.W.S., 1945. *The Theory of Sound*. Dover publications, New York.
- Reeder, D.B., Joseph, J.E., Rago, T.A., Bullard, J.M., Honneger, D., Haller, M.C., 2022. Acoustic spectrometry of bubbles in an estuarine front: Sound speed dispersion, void fraction, and bubble density. *J. Acoust. Soc. Am.* 151 (4), 2429–2443. <http://dx.doi.org/10.1121/1.5009923>.
- Ross, T., Lavery, A.C., 2011. Acoustic scattering from density and sound speed gradients: Modeling of oceanic pycnoclines. *J. Acoust. Soc. Am.* 131 (1), E54–E60. <http://dx.doi.org/10.1121/1.3669394>.
- Ross, T., Lueck, R., 2003. Sound scattering from oceanic turbulence. *Geophys. Res. Lett.* 30 (6), <http://dx.doi.org/10.1029/2002GL016733>.
- Rouse, H., 1939. Experiments on the mechanics of sediment suspension. In: *Proceedings 5th International Congress on Applied Mechanics*. John Wiley & Sons.
- Scully, M., 2016. The contribution of physical processes to inter-annual variations of hypoxia in Chesapeake Bay. *Limnol. Oceanogr.* 61 (6), 2243–2260. <http://dx.doi.org/10.1002/lno.10372>.
- Seim, H.E., 1999. Acoustic backscatter from salinity microstructure. *J. Atmos. Ocean. Technol.* 16 (11), 1491–1498. [http://dx.doi.org/10.1175/1520-0426\(1999\)016<1491:ABFSM>2.0.CO;2](http://dx.doi.org/10.1175/1520-0426(1999)016<1491:ABFSM>2.0.CO;2).
- Seim, H.E., Gregg, M.C., Miyamoto, R.T., 1995. Acoustic backscatter from turbulent microstructure. *J. Atmos. Ocean. Technol.* 12 (2), 367–380. [http://dx.doi.org/10.1175/1520-0426\(1995\)012<0367:ABFTM>2.0.CO;2](http://dx.doi.org/10.1175/1520-0426(1995)012<0367:ABFTM>2.0.CO;2).
- Simmonds, E., MacLennan, D., 2005. *Fisheries Acoustics, second ed.* Blackwell Science, Oxford, UK.
- Simpson, A.J., 2021. *Radar and Optical Remote Sensing of Submesoscale Frontal Features* (Ph.D. thesis). Oregon State University.
- Simpson, J.H., Nunes, R.A., 1981. The tidal intrusion front: An estuarine convergence zone. *Estuar. Coast. Shelf Sci.* 13 (3), 257–267. [http://dx.doi.org/10.1016/S0302-3524\(81\)80024-2](http://dx.doi.org/10.1016/S0302-3524(81)80024-2).
- Stanton, T.K., 1983. Multiple scattering with applications to fish-echo processing. *J. Acoust. Soc. Am.* 73 (4), 1164–1169. <http://dx.doi.org/10.1121/1.389287>.
- Stanton, T.K., 1984. Effects of second-order scattering on high resolution sonars. *J. Acoust. Soc. Am.* 76 (3), 861–866. <http://dx.doi.org/10.1121/1.391310>.
- Stranne, C., Mayer, L., Jakobsson, M., Weidner, E., Jerram, K., Weber, T.C., Anderson, L.G., Nilsson, J., Björk, G., Gårdfeldt, K., 2018. Acoustic mapping of mixed layer depth. *Ocean. Sci.* 14, 503–514. <http://dx.doi.org/10.5194/os-14-503-2018>.
- Stranne, C., Mayer, L., Weber, T.C., Ruddick, B.R., Jakobsson, M., Jerram, K., Weidner, E., Nilsson, J., Gårdfeldt, K., 2017. Acoustic mapping of thermohaline staircases in the Arctic Ocean. *Sci. Rep.* 7, 15192. <http://dx.doi.org/10.1038/s41598-017-15486-3>.
- Terrill, E.J., Melville, W.K., 2000. A broadband acoustic technique for measuring bubble size distributions: Laboratory and shallow water measurements. *J. Atmos. and Ocean. Technol.* 17 (2), 220–239. [http://dx.doi.org/10.1175/1520-0426\(2000\)017<0220:ABATFM>2.0.CO;2](http://dx.doi.org/10.1175/1520-0426(2000)017<0220:ABATFM>2.0.CO;2).
- Terrill, E.J., Melville, W.K., Stamski, D., 2001. Bubble entrainment by breaking waves and their influence on optical scattering in the upper ocean. *J. Geophys. Res.* 106 (C8), 16815–16823. <http://dx.doi.org/10.1029/2000JC000496>.
- Thomson, J., 2012. Wave breaking dissipation observed with “SWIFT” drifters. *J. Ocean. Atmos. Tech.* 29 (12), 866–882. <http://dx.doi.org/10.1175/JTECH-D-12-00018.1>.
- Thomson, J., Moulton, M., de Klerk, A., Talbert, J., Guerra, M., Kastner, S., Smith, M., Schwendeman, M., Zippel, S., Nylund, S., 2019. A new version of the SWIFT platform for waves, currents, and turbulence in the ocean surface layer. In: *2019 IEEE/OES Twelfth Current, Waves and Turbulence Measurement (CWTM)*. pp. 1–7. <http://dx.doi.org/10.1109/CWTM43797.2019.8955299>.
- Thorne, P.D., Hurther, D., 2014. An overview on the use of backscattered sound for measuring suspended particle size and concentration profiles in non-cohesive inorganic sediment transport studies. *Cont. Shelf Res.* 73, 97–118. <http://dx.doi.org/10.1016/j.csr.2013.10.017>.
- Thorne, P.D., MacDonald, I.T., Vincent, C.E., 2014. Modelling acoustic scattering by suspended flocculating sediments. *Cont. Shelf Res.* 88, 81–91. <http://dx.doi.org/10.1016/j.csr.2014.07.003>.
- Thorne, P.D., Vincent, C.E., Hardcastle, P.J., Rehman, S., Pearson, N., 1991. Measuring suspended sediment concentrations using acoustic backscatter devices. *Mar. Geo.* 98 (1), 7–16. [http://dx.doi.org/10.1016/0025-3227\(91\)90031-X](http://dx.doi.org/10.1016/0025-3227(91)90031-X).
- Thorpe, S.A., 1982. On the clouds of bubbles formed by breaking wind-waves in deep water, and their role in air-sea gas transfer. *Phil. Tran. R. Soc. Lond. A* 304, 155–210. <http://dx.doi.org/10.1098/rsta.1982.0011>.
- Thorpe, S.A., 2007. *An Introduction to Ocean Turbulence*. Cambridge University Press, <http://dx.doi.org/10.1017/CBO9780511801198>.
- Thorpe, S.A., Brubaker, J.M., 1983. Observations of sound reflection by temperature microstructure. *Limnol. Ocean.* 28 (4), 604–613. [http://dx.doi.org/10.1175/1520-0426\(1994\)011<1273:SOOLCA>2.0.CO;2](http://dx.doi.org/10.1175/1520-0426(1994)011<1273:SOOLCA>2.0.CO;2).
- Thorpe, S.A., Cure, M.S., Graham, A., Hall, A.J., 1994. Sonar observations of Langmuir circulation and estimation of dispersion of floating particles. *J. Atmos. Ocean. Technol.* 11 (5), 1273–1294. [http://dx.doi.org/10.1175/1520-0426\(1994\)011<1273:SOOLCA>2.0.CO;2](http://dx.doi.org/10.1175/1520-0426(1994)011<1273:SOOLCA>2.0.CO;2).
- Thorpe, S.A., Osborn, T.R., Farmer, D.M., Vagle, S., 2003. Bubble clouds and Langmuir circulation: observations and models. *J. Phys. Ocean.* 33 (9), 2013–2031. [http://dx.doi.org/10.1175/1520-0485\(2003\)033<2013:BCALO>2.0.CO;2](http://dx.doi.org/10.1175/1520-0485(2003)033<2013:BCALO>2.0.CO;2).
- Trevorrow, M.V., 2003. Measurements of near-surface bubble plumes in the open ocean with implications for high-frequency sonar performance. *J. Acoust. Soc. Am.* 114 (5), 2672–2684. <http://dx.doi.org/10.1121/1.1621008>.
- Trump, C.L., Marmorino, G.O., 2003. Mapping small-scale along-front structure using ADCP acoustic backscatter range-bin data. *Estuaries* 26 (4A), 878–884. <http://dx.doi.org/10.1007/BF02803346>.
- Vagle, S., Farmer, D.M., 1992. Measurements of bubble-size distributions by acoustical backscatter. *J. Ocean. Atmos. Technol.* 9 (5), 630–644. [http://dx.doi.org/10.1175/1520-0426\(1992\)009<0630:TMOBSD>2.0.CO;2](http://dx.doi.org/10.1175/1520-0426(1992)009<0630:TMOBSD>2.0.CO;2).
- Vagle, S., Farmer, D.M., 1998. A comparison of four methods for bubble size and void fraction measurements. *IEEE J. Ocean. Eng.* 23 (3), 211–222. <http://dx.doi.org/10.1109/48.701193>.
- Warren, J.D., Stanton, T.K., Wiebe, P.H., Seim, H.E., 2003. Inference of biological and physical parameters in an internal wave using multiple-frequency, acoustic-scattering data. *ICES J. Mar. Sci.* 60 (5), 1033–1046. [http://dx.doi.org/10.1016/S1054-3139\(03\)00121-8](http://dx.doi.org/10.1016/S1054-3139(03)00121-8).
- Weidner, E., Stranne, C., Hentati Sundberg, J., Weber, T.C., Mayer, L., Jakobsson, M., 2020. Tracking the spatiotemporal variability of the oxic–anoxic interface in the Baltic Sea with broadband acoustics. *ICES J. Mar. Sci.* 77 (7–8), 2814–2824. <http://dx.doi.org/10.1093/icesjms/fsaa153>.
- Weidner, E., Weber, T.C., 2021. An acoustic scattering model for stratification interfaces. *J. Acoust. Soc. Am.* 150 (6), 4353–4361. <http://dx.doi.org/10.1121/10.0009011>.
- Whipple, K., 2004. 12.163/12.463 surface processes and landscape evolution: Course notes. URL: <https://ocw.mit.edu/courses/12-163-surface-processes-and-landscape-evolution-fall-2004/pages/lecture-notes/>.
- Wood, A.B., 1930. *A Textbook of Sound, first ed.* MacMillan, New York.
- Wright, L.D., Coleman, J.M., 1971. Effluent expansion and interfacial mixing in the presence of a salt wedge, Mississippi River delta. *J. Geophys. Res.* 76 (36), 8649–8661. <http://dx.doi.org/10.1029/JC076i036p08649>.
- Yakuwa, I., Ohtani, M., 1969. Longitudinal distribution of surface salinity in an estuary. *Bull. Fac. Eng., Hokkaido Univ.* 54, 135–141.
- Yankovsky, A.E., Chapman, D.C., 1997. A simple theory for the fate of buoyant coastal discharges. *J. Phys. Ocean.* 27 (7), 1386–1401. [http://dx.doi.org/10.1175/1520-0485\(1997\)027<1386:ASTFTF>2.0.CO;2](http://dx.doi.org/10.1175/1520-0485(1997)027<1386:ASTFTF>2.0.CO;2).
- Young, R.A., Merrill, J.T., Clarke, T.L., Proni, J.R., 1982. Acoustic profiling of suspended sediments in the marine bottom boundary layer. *Geophys. Res. Lett.* 9 (3), 175–178. <http://dx.doi.org/10.1029/GL009i003p0175>.